# Simulation of a Portable Microwave Breast Cancer Detection System and Derivation of a Mathematical Model for the Relative Electromagnetic Fields

by

Debarati Nath

A thesis
submitted to the Faculty of Graduate Studies of
the University of Manitoba
in partial fulfillment of
the requirements for the degree of

**Master of Science**

Department of Biomedical Engineering
University of Manitoba
Winnipeg, Manitoba, Canada, 2021

## Author's Declaration For Electronic Submission Of A Thesis

I hereby declare that I am the sole author of this thesis. This is a true copy of the thesis, including any required final revisions, as accepted by my examiners.

I authorize the University of Manitoba to lend this thesis to other institutions or individuals for the purpose of scholarly research.

I further authorize the University of Manitoba to reproduce this thesis by photocopying or by other means, in total or in part, at the request of other institutions or individuals for the purpose of scholarly research.

I understand that my thesis may be made electronically available to the public.

**SIMULATION OF A PORTABLE MICROWAVE BREAST CANCER DETECTION SYSTEM AND DERIVATION OF A MATHEMATICAL MODEL FOR THE RELATIVE ELECTROMAGNETIC FIELDS**

Debarati Nath

Master of Science

Biomedical Engineering

University of Manitoba, 2021

## Abstract

Breast microwave imaging (BMI) systems open a new era for detecting breast cancer because of their advantages like non-ionizing radiation and cost-effectiveness. However, Low- and Middle-Income countries (LMIC) have limited options to make frequent accesses for those existing microwave breast cancer detection devices. This study worked on the simulated microwave breast cancer detection system to make the microwave device portable, and user-friendly. The proposed portable system with a transmitter, a sensing chamber, and a receiver array was simulated in the CST Microwave solver. A horn antenna used as the transmitter was designed using the same characteristics of the horn antenna used in the laboratory and a 90% bandwidth agreement at -10dB between the simulated and measured reflection coefficient was acquired. 37 points on the receiver array were used instead of designing independent antennas as receivers for avoiding design complexities. The effects of a point-like scatterer (Al rod) on the relative electromagnetic (EM) fields were analyzed to improve the design and performances of the portable system. The ratios of E-field intensities to the open-space E-field intensities were evaluated as a function of frequencies and rod positions in the sensing chamber. A mathematical equation was derived to explain the characteristics of the relative EM strength because of the presence of the Al rod. A robust multi-dimensional fitting procedure was used to establish an agreement of -1.3% $\pm$ 10% between the fitted and simulated data. $r^2$ = 0.92 with p $<$ 0.01 was obtained for rod positions within $\pm$ 6 cm in both x and y- directions and frequencies from 2-8 GHz. The values of parameters of the proposed mathematical equation were evaluated and the theoretical explanations were established. The analytical approach with the analysis on EM field strength with rod positions will allow to produce data for transfer learning of machine learning networks and enable optimal antenna placement.

# Contribution

The contributions of the author are written in the below for completing her M.Sc. degree at the Non-Ionizing Laboratory at the University of Manitoba.

- Design a horn antenna to be used as a transmitter for the portable microwave breast cancer detection system in Antenna Magus Software and CST Microwave Solver
- Compare the characteristics (reflection coefficient, gain, VSWR, and return losses) of the antenna with the antenna used in the laboratory experiment.
- Design and simulate the portable microwave system with a transmitter, the sensing chamber, and the receiver array with 37 receiver points in CST Microwave Software.
- Simulate the portable system with a point-like scatterer as a function of the frequency and the position of the scatterer inside the sensing chamber.
- Evaluate the effects of a point-like scatterer on the electric fields in the portable device.
- Understand the behaviors of the scatterer on the relative electric field strength as a function of frequency and the position of the scatterer.
- A mathematical equation was developed with the help of Dr. Pistorius to describe the received electric fields and the parameters were evaluated using a robust multi-dimensional fitting procedure.

# Acknowledgments

I would like to convey my gratitude to my supervisor, Dr. Stephen Pistorius for his support throughout my M.Sc. degree, and for always encouraging me to push for the best. I want to appreciate my M.Sc. committee members time and support. Many thanks to my parents for their unwavering support throughout both my academic and personal life and nothing is possible without them. Special thanks to my elder brother and my spouse for being always with me and their suggestions and advices that helped me to keep quiet and focused to complete my M.Sc. degree. I am thankful to my colleagues from Non-ionizing laboratory. I am grateful to Mario Solis, one of the colleagues from the Non-ionizing research laboratory for his support and guidelines which helped me to start my M.Sc. career as an International student. Thanks to all graduate stuffs from Biomedical Engineering Department and Department of Physics and Astronomy.

# Dedication

*I want to dedicate my thesis to my beloved parents because nothing is possible without their love and support. I also want to dedicate my thesis to my M.Sc. supervisor - Dr. Stephen Pistorius*

# Contents

# List of Tables

# List of Figures

# Chapter 1

# Introduction

This chapter provides a background to breast cancer worldwide and Canadian incidence and mortality rates, as well as the challenges associated with increased mortality rates in Low and Middle-Income Countries (LMIC) and even in remote regions of developed nations. The conventional breast cancer detection modalities are described and the microwave system is introduced as a prospective device for detecting breast cancer. Finally, this chapter will cover the numerous microwave sensing tools and concludes with the potential advantages of a breast microwave sensing device.

## 1.1 Background and Problem Context

### 1.1.1 Nature of Breast Cancer

Cancer, one of the root causes of death annually accounts for 10 million deaths and 19.3 million people affected by cancer worldwide [1]. The Canadian Cancer Society projects that 1 in 2 Canadians will develop cancer at some point in their life, with 1 in 4 Canadians dying from cancer [2]. Breast cancer, one of the most frequent forms of cancer in women is responsible for 684,996 deaths worldwide [3]. The International Agency for Research on Cancer reports that globally, 1 in 4 women will be diagnosed with breast cancer [1]. On average, in Canada, 75 Canadian women get treatment for breast cancer each day, and 14 Canadian women die each day from this disease [4].

The breast cancer incidence rate is higher in developed countries than in low income and developing countries [5]. The age-standardized incidence rate is more than 95.5 per 100,000 in Australia, and New Zealand [5] while the age-standardized incidence rate is 33.0 - 50.4 per

100,000 in Eastern Africa, Eastern Asia, and South Africa [5]. However, the breast cancer mortality rate for developing and low-income countries is higher than the mortality rate of developed countries. The age-standardized mortality rate due to breast cancer is estimated to be between 18.0 and 22.3 per 100,000 for Middle Africa, Northern Africa, and Western Africa, whereas Australia, and New Zealand has a mortality rate of approximately 12.1 per 100,000 [5].

In Canada, a 60% mortality-to-incidence rate is found in rural areas of Manitoba while urban Manitoba has approximately a 37% mortality-to-incidence rate [6].

When some cells in breasts change and divide in an uncontrolled way, breast cancer occurs [5]. Although the root causes of the uncontrolled division of breast cells are not fully understood, the incidence of breast cancer varies from country to country depending on the life expectancy, the growth of urbanization, the change of lifestyles, and early detection [7]. Since early-stage breast cancer usually may not result in any symptoms, early detection of breast cancer is required if curative treatment is to be provided. Therefore, if it is possible to detect cancer early, the overall survival rate can be increased [8, 9], and the volume of treatment will be minimized.

### 1.1.2 Traditional Breast Cancer Detection Modalities

Screening is commonly used to detect early-stage breast cancer. Among various breast cancer detection systems, X-ray mammography is considered as a gold standard [10, 11], but X-ray mammography has limitations. In Canada, a risk-benefit analysis of X-ray mammography has identified that the potential benefits of X-ray mammography as a breast cancer screening technique only apply to women above 50 years of age [12]. When the mammography is performed, the breast needs to be compressed between 2 plastic plates [13]. During the examination, this breast compression process is uncomfortable for many women. In addition, 42.9 – 43.1% of American women between the ages of 40 – 74 have dense breasts [14]. Healthy human breasts consist of adipose tissues, fibroglandular tissues, milk ducts, and connective tissues [15]. Dense breasts have more dense tissues like connective tissues, glands, and milk ducts than fatty tissues. The dense breast tissues provide solid white areas on mammograms and hence, the experts face difficulties to see through the solid white areas [16, 17]. There is a 20 - 60% cumulative risk of a false-positive rate after ten (10) mammograms [18]. The consequences of false positives increase the potential for unnecessary diagnosis procedures, including further diagnostic imaging or an invasive biopsy [19]. These

follow-up activities may create stress, anxiety and increase healthcare costs. Although mammography uses low doses of radiation, repeated exposure to X-rays can increase the risk of radiation carcinogenesis [20].

Another breast cancer detection technique is Ultrasound that utilizes non-ionizing high-frequency sound waves for detecting cancerous lesions and provides a 65.5% specificity rate [21, 22]. However, Ultrasound has a higher false-positive rate than mammography [23] and requires an experienced person for operating and interpreting the images [24]. Ultrasound can, however, increase the diagnostic sensitivity when used as a follow-up modality after mammography [14].

Magnetic Resonance Imaging (MRI) provides a non-ionizing method and delivers 75% sensitivity [25, 26]. The sensitivity of MRI is higher than the sensitivity of X-ray mammography [25, 26]. However, MRI has a broad specificity range which is between 37% to 97% because of the intensification of both benign and malignant lesions [27]. MRI also needs a longer time for the assessment and is unsuitable for claustrophobic patients [28]. Hence, the high capital and operating cost, limited availability, longer assessment period, and challenges with specificity make MRI unsuitable to use as a breast screening device [28].

### 1.1.3 Characteristics of Ideal Breast Cancer Detection System

The drawbacks of the conventional breast cancer detection techniques have inspired the improvement of the existing breast imaging modalities [9] and the invention of new approaches [29]. The Institute of Medicine (IOM) has identified the characteristics for an ideal breast cancer detection system [19, 30, 31]. These are as follows -

- limited health risk
- simple, flexible, and available
- cost-effective, non-invasive, easy to interpret, and consistent results
- sensitive to tumours and specific to malignancies
- enable to detect the breast cancer lesions at a treatable stage
- comfortable for women

The breast imaging process should provide a contrast that enables to identify the difference between the tumorous cell and other breast cells. Microwave systems can deliver this electrical property contrast to detect small breast cancer lesions [19]. Different properties of microwave systems similar to the properties of an ideal breast cancer detection system permit microwave systems to use as a breast cancer detection modality with the potential to deliver clinically validated high specificity and sensitivity.

## 1.2 Background of Breast Microwave Imaging

Microwave imaging techniques have numerous applications including observing liquids in the lungs, the bladder's urine volume, as well as detecting bone lesions, brain hemorrhages, and breast cancer [32]. Microwave has been investigated for detecting breast cancerous lesions for over two decades [31,33,34]. Microwave-based systems identify the presence of a breast lesion by producing a contrast image between the malignant and the other breast cells using the backscattering of electromagnetic signals within the microwave energy range.

### 1.2.1 Characteristics of Microwave Imaging System

Microwave technologies have the following promising qualities that allow it as a breast cancer detection modality.

- Microwave technologies use non-ionizing radiation.
- Microwave systems are comfortable for women because the systems do not use breast compression during the examination.
- Instead of using ionizing radiation, microwave systems use various physical characteristics such as tissue elasticity, temperature, and electrical properties to detect breast lesions [19].
- Microwave systems provide high contrast because of the difference in dielectric properties between healthy and malignant breast tissues [35]
- Microwave modalities can be robust, provide a high detection rate, and offer low cost.

- Microwave radiation can penetrate to about 100 mm depth in soft tissue, consistent with the breast radius. The location of other human organs like liver or kidneys are such that microwaves have inadequate penetration [36].

- Unlike many other human organs, human breasts are not overlaid with layers of muscle. This property of breasts leads to lower scattering and signal attenuation. Breasts can also be probed from different angles [32]. As a result, an array of antennas for the radar-based microwave system which is surrounded the breast can record the transmitted and backscattered reflections and create a reflection map that can be displayed as an image [37].

### 1.2.2 Conventional Breast Microwave Imaging Devices

There are three common forms of hardware set-ups for breast microwave imaging modalities. They are passive, hybrid, and active methods. The passive microwave imaging techniques use radiometers to estimate the temperature differences in the breast [19, 31]. Due to tumors, the temperature of the breast increases. Passive methods detect tumors by measuring the increased breast temperature compared to the healthy breast. Microwave radiometries that use the passive microwave methods have been investigated for breast cancer detection for decades [19]. The radiometry systems produce images that represent the temperature estimated over a quadrant of the breast. At the time of diagnosis, the produced image helps to compare the specific breast lesion's area with the corresponding area of the other healthy breast [19].

Hybrid microwave imagings, known as microwave-induced ultrasonic imagings have also been developed to detect breast cancer. Due to higher conductivity, tumors absorb more energy inside the breast compared to other breast tissues. Hybrid measurements use this property of the malignant breast tissue for breast cancer detection. The hybrid microwave-acoustic imaging method heat breast tissues repeatedly and selectively with the help of microwave energy. The breast tissues which have higher conductivity such as tumor tissue can enlarge due to heating. The tissue expansions and shrinkings because of the microwave-induced heating and subsequent cooling generate acoustic waves which are then detected by Ultrasound transducers [19, 31].

Active microwave systems illuminate the breast with microwaves to measure the transmitted and reflected microwave signals [19, 31]. Numerous active microwave techniques (tomography,

chirp-pulse microwave computed tomography, holography, pulsed radar, etc.) are used to detect the tumor's presence inside the breast [31].

Microwave tomography generates a map of the electrical properties of the scanned breast tissues. The image is reconstructed by the measured spatial distribution of the dielectric constant and / or conductivity [19]. An iterative process that matches the measured and computed data is required to reconstruct the image. This highly ill-posed inverse scattering problem for reconstructing the image requires apriori information and significant computational resources to reconstruct the dielectric properties.

Radar-based microwave imaging develops images focused on the location of strongly scattering objects by interrogating the breast tissues with an incident microwave field. When the radar-based microwave technique transmits the microwave signal through the breast tissues, the tissues produce a scattered field due to the incident field [38]. The radar-based microwave systems measure this resultant field.

The interaction of the transmitted electromagnetic field with the breast tissues can, in principle, be described by the complex dielectric constant $\epsilon$ completely [38].

$$\epsilon = \epsilon' + j\epsilon'' \tag{1.1}$$

where $\epsilon'$ and $\epsilon''$ are the real (conductivity) and imaginary (permittivity) parts of the dielectric constant, respectively. The relative dielectric constant ($\epsilon_r$) is more appropriate to describe the dielectric differences among the healthy and cancerous cells [39].

$$\epsilon_r = \frac{\epsilon}{\epsilon_0} = \epsilon_0(\epsilon_r{}' + j\epsilon_r{}'') \tag{1.2}$$

This dielectric difference provides a contrast that helps to compare the breast cancer lesions and other healthy breast tissues. Higher contrast between fibroglandular tissues and tumors may result in high specificity which results in a lower false-positive rate.

Confocal microwave imaging has also been explored as a recent way to detect breast lesion. The confocal imaging techniques estimate the location and presence of the significant scatterers in the breast rather than discover the dielectric properties of the breast [19, 31].

When the generated microwave radiation couples with the breast tissues, the active microwave modalities detect microwave scattered signals and process the signals to detect the tumor's presence inside the breast. However, the hardware set-ups of the active microwave modalities can be varied due to the following factors [31].

- The positioning of the patients can be either prone or supine when the patients are lying or the patients can also be standing during the time of data collection.
- The breast can be placed in the chamber of coupling liquids, or in constraining cup of desired sizes and shapes.
- The surface where the data are acquired can be planer, cylindrical, and hemispherical.
- The various characteristics like time-domain or frequency-domain can be used for acquiring the signals.

### 1.2.3 Methodology of Breast Microwave Imaging for Detecting Cancer

Active microwave technique of breast imaging system uses the electrical properties of the breast tissues to detect cancer. The electrical properties of a living cell are permittivity and conductivity. The cell's water content and presence of ionized molecules will impact the electrical properties of the cell. The permittivity correlates with the water content in the cell whereas conductivity explicitly depends on the presence of ionizing molecules such as salt [31]. By virtue of the increase of angiogenesis (growth of blood vessels), malignant tumors contain higher water concentrations and create greater permittivity than normal breast tissues [39]. Hence, any cancer cell has a higher permittivity due to higher water content than the permittivity of healthy breast cells [39]. Microwave techniques apply the differences of the permittivity between the tumors and other breast tissues to detect malignant regions.

The differences in the permittivity due to cancerous cells in the breast provide a contrast that can be measured and displayed. The contrast is frequency-dependent and decreases at higher frequencies. A 2002 study identified a contrast of 10:1 between the breast tumors and healthy tissues [40] although a later study clarified that this high contrast had only applied between adipose tissue and tumor [40]. While the 2002 study also reported a contrast between fibroglandular tissue

and tumor of less than 40%, this contrast is still an order of magnitude larger than the contrast of X-ray mammography [40]. The significance of the measured contrast encouraged researchers to investigate microwave-based breast cancer detection systems further. The ongoing research on the dielectric properties with ex-vivo measurement demonstrated that the dielectric properties of the cancerous cells were six times greater than those of fatty tissues and 1.5 times higher than fibroglandular tissues in the frequency range of 0.5 GHz to 20 GHz [40]. This study delivered the contrast between 8% to 10% [41] while X-ray mammography reported lower contrast of 4% - 10% [31].

Since breast microwave sensing (BMS) systems provide a high contrast ratio and good cost-effectiveness, many BMS systems have been developed for clinical operation [42, 43, 44, 45, 46]. Many research groups have conducted their initial research experiments with phantoms and with limited clinical trials. To localize tumors in the breast, the researchers have also applied numerous algorithms, including model-based image recognition technique, confocal microwave imaging technique, multiplicative delay and sum, and holographic approaches [47, 48].

### 1.2.4 Advantages of Breast Microwave Sensing Systems

The breast microwave sensing (BMS) system provides a promising alternative for clinical breast cancer detection with several potential advantages. First of all, the BMS systems minimize cost, and hence, the systems may be available for Low- and Middle-income countries (LMIC). The systems employ non-ionizing radiation. These low-power and non-invasive techniques would enable the patients to safely carry out more repeated examinations [49]. As no breast compression is needed for microwave-based breast cancer detection tools [19], the patients feel comfortable using the microwave sensing system. Microwave techniques benefit from delivering a clinically validated high specificity and sensitivity compared to X-ray mammography. As a result, the BMS systems are considered to open a new path for mass population breast cancer screening [31].

### 1.2.5 Disadvantages of Breast Microwave Sensing Systems

The clinically established BMS systems face several disadvantages even though these systems have been established as complementary modalities for the detection of breast cancer. Microwave imaging technologies typically require a single frequency band (or a series of stepped frequen-

cies) to minimize the complexity of the model and need significant computational resources [50]. Microwave technologies also provide deficiency in the resolution of the reconstructed images especially in the fibroglandular region [31, 51]. The relative volume of fibroglandular tissue inside the breast (breast density) produces challenges to detect the tumor [52]. In addition, there is still a need for an experienced person to inspect the images that have been reconstructed from the conventional BMS systems. Microwave tomography and radar-based systems are two common conventional BMS modalities in microwave technologies for breast cancer detection and both systems have their disadvantages.

Tomography-based microwave technology cannot reliably reconstruct the dielectric profile from non-linear and ill-posed data without prior information [52]. Recent microwave tomography systems are computationally costly and take a longer period to reconstruct the images [37, 50]. Because of taking a long time to take larger data, the motion of the patient can produce blur images and decreases the sensitivity and resolution of the imaging procedure [31].

Radar-based microwave approaches do not attempt to reconstruct the dielectric properties of the tissues but focus on detecting an abnormally large scattering response associated with a tumor. However, radar-based sensing systems experience significant signal attenuation. The radar-based microwave systems also face difficulties to detect tumors because of the effects of electromagnetic scattering, challenges of determining frequency range, breast tissue heterogeneity, and dispersion within the breast [31]. The air radar-based detection tools encounter low image contrast primarily due to the fibroglandular tissues [53].

## 1.3 Thesis Structure

Literature review and problem statement for this thesis are included in **Chapter 2**. The design of the simulated portable breast cancer detection system with the design of a horn antenna as the transmitter is demonstrated in **Chapter 3**. The behaviors of the electromagnetic fields on account of the point-like scattering object are narrated in **Chapter 4** and the analytical approach to describe the E-fields responses as a result of the scattering entity are provided in **Chapter 5**. Conclusion and future work of this thesis are included in **Chapter 6**.

## 1.4 Conclusion

This chapter explores the global breast cancer situation with Canadian breast cancer state and provides the link between the availability of breast cancer detection devices and the mortality rate of Low- and Middle-Income countries. The traditional breast cancer detection systems are introduced and the problems associated with the traditional breast cancer detection modalities are also investigated. The properties of an ideal breast cancer detection tool are included. Finally, this chapter provides the advantages of microwave technologies to detect breast lesions and concludes with the methodology of detecting breast cancerous lesions using microwave tools.

# Chapter 2

# Literature Review and Problem Statement

This chapter provides the details of the hardware and software setups of some existing breast cancer detection systems. The main purpose of this chapter is to understand electromagnetic tools, simulation approaches, and hardware techniques used in the existing microwave breast cancer detection modalities and the problems of implementing the existing microwave sensing system in remote regions. For remote regions, the literature reviews and problem statements of this chapter help to determine the simulation procedure for the proposed portable microwave breast cancer detection system under development in the lab. Finally, this chapter presents the research question and concludes with the objectives of this thesis.

## 2.1 Literature Review - Clinical Microwave Breast Cancer Microwave System

Much research on Breast Microwave Sensing (BMS) systems has been based on simulations and phantom scans. However, the success of any biomedical device ultimately depends on clinical results. To date, only a limited number of BMS research groups have carried out published clinical trials. The research groups are Dartmouth College, University of Bristol, University of Calgary, McGill University, and University of Manitoba [32, 37, 43, 44, 45, 46, 54, 55, 56]. The technical aspect of BMS tools chosen by these research groups, such as the number and type of antennas, the operating frequency range, the image reconstruction algorithms used as the forward solvers, and the hardware setup, are reviewed and presented in the following subsections.

### 2.1.1 Dartmouth College

The research groups from Dartmouth College, USA, described a prototype breast cancer detection system where a near-field microwave approach was used for breast imaging [43]. The system which operated from 0.5 GHz to 2.9 GHz used sixteen (16) transceiving monopole antenna arrays where the antenna array was connected to a 16-channel switching matrix and a digital radio frequency generator. The antenna array was immersed in a chamber filled with water and glycerine mixture. The water and glycerine mixture was used as a coupling medium to reduce the reflections from the skin surface. A motor-controlled system moved the antennas to different heights within the illumination chamber [43].

The system consisted of two interleaved antenna sub-arrays and eight antennas were located in each sub-array [43]. Each of the antennas transmitted sequentially the electromagnetic signals to the other 15 antennas for a total of 240 data points at each frequency. For each plane, 2D coronal slices were generated by the simultaneous movement of the antenna sub-arrays. The measurements in a cross-plane configuration generated the 3D images [43].

In ongoing research work, the research group developed a 3rd generation of the detection system [55]. The developed system used an updated motion-controlled system to move the antenna sub-arrays to numerous in-plane and cross-plane positions within the chamber. A 3D iterative Gauss-Newton algorithm using Finite-Difference Time-Domain (FDTD) method was applied to reconstruct the images from the microwave measurements. Following that, the research group explored an alternating-direction implicit (ADI) FDTD approach to increase the speed of the process and reduce the computation time [57].

### 2.1.2 University of Calgary – TSAR

The University of Calgary developed its first clinical prototype for breast cancer detection in 2021, using a monostatic radar-based imaging system called Tissue Sensing Adaptive Radar (TSAR) [54]. This system has a padded table with a hole where the patients can place breasts into a cylindrical container filled with canola oil. The canola oil provided the matching between the breast skin and a sensor attached to a positioning arm. The arm scanned the breast by moving vertically with the rotation of the tank [54]. A laser was mounted to the positioning arm to record the breast

outline, and a camera mounted on the chamber's side captured images to monitor the imaging procedure [54]. The imaging system used a custom Balanced Antipodal Vivaldi Antenna with a Dielectric Director (BAVA-D) [58]. The operating bandwidth of the antenna was from 2.4 GHz to 12 GHz to produce an image of the breast lesion. The subject lay in the prone position on the bed of the imaging system which had a 130 mm opening for the subject's breast and the breast was immersed into the canola oil inside the chamber. The system took 30 minutes to scan 200 positions and the image was reconstructed using an FDTD algorithm. The research group simulated the entire process to validate their experimental modality [58].

For clinical validation, the research group conducted a trial with eight patients [44]. They compared Microwave images with mammograms, magnetic resonance scans, and biopsies. Images reconstructed by the TSAR responded consistently with the location of the malignant lesion for one of three patients for whom cancerous tumors were identified visibly [44].

### 2.1.3 University of Bristol – MARIA M4

The research group at the University of Bristol initially built a breast cancer detection device with 16 antenna array elements and then developed the system with a 31-element Ultra-wideband (UWB) slot antenna system (MARIA M3) [46]. In MARIA M4, they improved the image reconstruction and reduced the scanning time by developing a 60 wide-slot antenna element array system [46,59]. The entire imaging system was arranged around a hemispherical cup made of acrylonitrile butadiene styrene (ABS) plastic. The operating frequency of the MARIA M4 system was from 3 GHz to 8 GHz [46]. The research group used a separate fixed coupling shell between the antennas and the breast tissue filled with water or an oil-based coupling fluid with a dielectric constant of 10. The advantages of using the coupling shell are -

- To interface the antenna to the tissue,
- To provide a fixed spacer to place the imaged tissue volume into the far-field of the antenna.

The coupling shell and coupling fluid also permitted the antenna array to rotate underneath the fixed shell. In the MARIA M4 system, the antenna array can be adjusted for the patients' comfort. The operator also balanced the subject's breast within the scanning cup by adjusting the antenna array instead of moving the subject [46]. The rotation of the system cabinet under the bed enabled

the introduction of additional inserts into the basic breast cup to accommodate smaller breast cup sizes. The research group used an advanced version of the Delay and Sum (DAS) beamforming approach for image reconstruction [46].

### 2.1.4 McGill University

The research group at McGill University developed a time-domain, multi-static radar-based microwave breast cancer detection system [56]. The system operated from 2 GHz to 4 GHz. The principal components of the system were an impulse generator, a clock, an oscilloscope, broadband antennas, and a radome [45]. The radome was a hemispherical dielectric bowl in which the subject's breast was placed. The exterior surface of this radome had 16 antennas. Ultrasound gel was used as the coupling liquid with a dielectric constant of 68 for filling the air gaps between the breast surface and the hemispherical radome [56]. By doing so, Ultrasound gel created a lossy medium that did not allow the transmission and reflection of signals to pass through the phantom directly. An off-the-shelf pulse generator produced pulses with full-width at the half-maximum duration of 70 ps which were further reshaped by a synthesized broadband reflector (SBR) and fed to the antenna array.

The system used the switching network to cycle through all antennas, selecting one antenna as a transmitter and the other 15 antennas as receivers. The transmitted microwave pulse scattered within the breast and the receiver antennas received the propagated signals, which were recorded by the oscilloscope [56]. The entire procedure was repeated until each antenna in the system array acted as a transmitter. For all possible antenna pairs, the system collected 240 signals from the scan of the breast. The measured signals were further filtered to reduce background noises and reflections. The research group applied a Delay-Multiply-and-Sum (DMAS) algorithm to reconstruct 3D images using the time-domain received signals [56].

### 2.1.5 University of Manitoba

The Non-ionizing research group at the University of Manitoba has developed two microwave systems for detecting breast cancer - a clinically validated and Health Canada registered medical device that uses a rotating bistatic radar configuration [42] and a portable breast cancer detection system for early breast cancer detection which has not yet been clinically validated [37].

The clinically validated breast microwave imaging system operated from 2 GHz to 8 GHz [32]. Two double-ridged horn antennas with a bandwidth from 2 GHz to 20 GHz were used as the antenna array. The antennas were placed on a circular rotating and lifting tabletop using a holder with 35, 145, or 180 degrees angular separation. The entire system operated in air and no coupling medium was used. The benefit of using an air medium was to make the system more clinically viable while reducing the mechanical complexity and losses associated with coupling liquids [37]. A two-port Planar Vector Network Analyzer (VNA) was used to record the propagated signals through the breast. A complete scan included three vertical planes with 144 antenna positions and took 1755 s to 1876 s to be recorded [37]. The system used a bed with an aperture of 17 cm to hold one breast of the subject so that the subject could lie in the prone position. The research group initially used a holographic approach [60] but more recently used an Iterative Delay and Sum method (iDAS) for obtaining the images [61]. The research group also showed that convolutional neural networks (CNN) could detect the breast lesion inside the subject's breast [38].

The portable breast cancer detection system had one horn antenna as a transmitter and 13 patch antenna as receivers [37]. The receiver antennas were located on a semi-circular platform with a 4 mm separation between antennas. The envelope correlation coefficient was measured to determine the optimal separation between the receiver antennas by limiting the mutual coupling between antennas in the receiver antenna array while maximizing the number of the antennas. The portable system transmitted electromagnetic signals from 1.5 GHz to 6 GHz. The system was calibrated using a $13\times10$ array of geometric correction constants, which was derived from the E-fields obtained from the simulated portable system (work done as part of this thesis). The differences between the simulated and experimental outcomes were between -4% to 3% for open space conditions and were $\pm15\%$ for different positions of the point-like scatters inside the portable system [37]. The portable system converted the RF signal to a DC voltage to detect changes in the fields due to scattering objects. The power ranges for the receiver antennas varied from 10.3 dBm to 9.3 dBm at a 95% Confidence Interval (CI) under open space conditions. The minimum and maximum average relative powers (ARP) were measured as -0.65 and 1.63 respectively.

### 2.1.6 Conclusion

The section introduces various breast cancer detection systems that have been used clinically to illustrate some different approaches that have been applied to date for detecting breast lesions. This review enables us to recognize the strengths and weaknesses of different methods and provides background to the issues which can be investigated in developing a portable system.

## 2.2 Literature Review - Types of Antennas in Microwave Breast Cancer Detection

### 2.2.1 Introduction

Detailed knowledge of microwave transmitters and receivers should be needed for designing a microwave breast cancer detection system. Various properties such as the geometry of the microwave antenna, the frequency range of the transmitted microwave signal, the number of sensors to detect the breast lesions should be reviewed. The research progress on microwave antennas in the breast cancer detection system should also be needed to investigate. This section introduces various microwave antennas used for breast cancer detection that has enabled us to recognize the advantages and limitations of different microwave antennas for the application of breast cancer detection. The background of designing microwave antennas and breast phantoms to detect the breast lesions in CST Microwave Solver is also provided for developing a simulated portable system in 3D environment.

### 2.2.2 Literature Review

The methodology and primary outcome of an ultra-wideband (UWB) microwave radar technology were introduced for the detection of early-stage breast cancer [62]. The system used three-dimensional (3D) Finite-difference Time-domain (FDTD) simulations. A resistively loaded bowtie antenna element of a proposed pulsed microwave confocal array was designed. The proposed antenna that was located at the surface of the breast had a flare length of h = 4 cm and a flare angle of 53°. The research group concluded that the UWB end reflections for the bowtie element could be reduced to 125 dB with the proper resistive loading. They also concluded that

the radiating bandwidth and backscatter dynamic-range characteristics of an optimized resistively loaded bowtie antenna element in conjunction with the existing microwave instruments were adequate for detecting early-stage tumors [62].

A low-profile and wideband stacked patch antenna was designed to detect breast cancer [51]. The antenna was simulated using FDTD, and a prototype of the antenna was designed to compare the measured results with the simulated results. The operating frequency for the proposed antenna was from 4 GHz to 9.5 GHz. The time-domain characteristics of the antenna were also included [51]. A phantom made of synthetic breast tissue was scanned to measure the radiation properties of the antenna. The research group immersed a prototype of the antenna in the breast tissue medium, and then, another identical second prototype was kept on the horizontal plane in the air-medium interface [51]. The research group concluded that the proposed antenna provided acceptable properties to use antenna for the short pulse radar application.

A cylindrical static multi-antenna arrangement with 32 horizontally oriented antennas was created for a 3-D microwave imaging system [63]. The method of moment (MoM) solver was used for the simulation. The system operated up to 3 GHz frequency. The antenna array that consisted of 32 horizontally oriented antennas was designed in a cylindrical fashion. The images were obtained using a non-linear inverse scattering-based image reconstruction algorithm that combined the moment forward solver method and the Newton minimization algorithm [63].

A wide-slot antenna was designed for use in a UWB antenna array for microwave breast cancer detection [64]. A prototype was built to compare the physically measured antenna characteristics with the simulated characteristics. The designed antenna was 3 times smaller than the stacked patch antenna designed previously for breast cancer detection purposes. The radiated pulses of the wide-slot antenna were almost identical (fidelity 95%) for angles up to 60° away from bore-sight, and images of the breast could be reconstructed with low levels of clutter by this antenna [64].

A planar antenna array was built with 12 corrugated tapered slot elements for use in an ultra-wideband biomedical microwave imaging system [65]. The slot elements were designed to be compact and have a low profile, moderate gain, and low distortion performance in the time domain. The radiators and the ground planes of the antennas were coated with a dielectric material to protect the antennas from the adverse effect of the coupling liquid [65]. Each antenna operated from 3.1 GHz to 10.6 GHz. The time-domain performances of the antennas allowed the antennas

to transmit and receive narrow pulses without distortion.

A side slotted vivaldi antenna for breast phantom measurement [66] was used. The proposed vivaldi antenna had additional six slots in the radiating fins for improving the frequency range from 1.54 GHz to 7 GHz. The addition of slots also reduced the sideband and increased the gain of the main lobe. These types of proposed addition developed various antenna properties like efficiency and radiation directivity [66].

### 2.2.3 Conclusion

This section introduces the geometries and methodology of detecting breast lesions using different microwave antennas. This review allows us to understand the geometries of different antennas and their methodology to detect breast tumors. This part of this thesis also enables us to interpret the advantages and disadvantages of different microwave antennas for the application of breast cancer detection. In describing these microwave antennas, this section demonstrates how the microwave antenna would be selected and which characteristics of the antenna should be considered for this thesis. This section also provides the basic idea on deciding the methodology to detect the breast lesions by using the selected microwave antenna for this thesis.

## 2.3 Literature Review - Microwave Breast Cancer Detection using CST Microwave Studio

### 2.3.1 Introduction

Detailed knowledge of the existing methodology of designing microwave antenna and breast phantom in a 3D simulator like CST Microwave Studio is needed before designing a new system for breast cancer detection. A review of the advantages and limitations of CST Microwave Studio should also be needed. This section provides the reviews on various breast cancer detection systems designed in CST Microwave Studio with the background of the microwave antenna and breast phantom. The methodologies of detecting the breast lesions that have also been investigated will enable to design the portable sensing system in CST Microwave Studio.

### 2.3.2 Literature Review

A hemispherical breast phantom with two microstrip patch antennas was designed in CST Microwave Studio [67]. The transmitter microstrip patch antenna was kept stationary, and the receiver microstrip antenna was moved to different positions from the bottom to the top of the breast structure. The antennas were circular pin-fed linearly polarized microstrip patch antennas for this preliminary study on microwave technology in breast cancer detection.

Another study simulated a hemispherical breast phantom with a monopole antenna using CST Microwave Studio [68]. The antenna formed a synthetic circular array around the breast phantom and transmitted signals at each position and received the back-scattering signal using a monostatic radar configuration.

In a further study, a breast cancer detection setup was simulated in the CST Microwave studio using a hemispherical breast phantom and two horn antennas [69]. The transmitter transmitted the plane wave and the receiver received the propagated signal on the other side of the breast phantom. The simulation was performed for breast phantoms of 10 different radii. The spherical tumors were covered with limestone and the limestone masses were placed inside the fibroglandular layer of the breast phantom. The Debye model was used to derive the dielectric properties of the breast phantom.

An approach that employed a reconstruction algorithm that combined wavelet transform with a neural network simulated with a three-dimensional heterogeneous breast model using CST Microwave Studio [70]. The simulated breast phantom included four structures; fibroglandular, milk ducts, fat, and connective tissues. A 1st order Debye dispersion model was used to calculate the dielectric properties of the breast phantom. The plane wave was transmitted through the breast tissue, and probes were used for receiving the transmitted signal in CST Microwave Studio.

Using CST Microwave Studio, another study simulated two UWB rectangular microstrip patch antenna and a hemispherical breast phantom [71]. A spherical tumor was designed with 50 F/m permittivities and 4 S/m conductivities. The proposed breast microwave system was simulated with and without canola oil. The simulated E-fields and reflection coefficient of the antenna were recorded, and data mining using a Random Forest algorithm was used to classify whether a tumor was present.

### 2.3.3 Conclusion

This section described different breast cancer detection systems that were designed in CST Microwave Studio. In describing these systems, this section reveals that CST Microwave Studio is a recognized and appropriate tool for carrying out 3D simulation and CST Microwave Studio will be the primary tool used in this research to design the transmitter antenna and the whole sensing system. Finally, this section investigates whether CST Microwave Studio can also be used to design the breast phantom consisting of breast lesions for the analysis purpose of this thesis in the future.

## 2.4 Problem Statement

### 2.4.1 Introduction

This section provides the problems of implementing the microwave sensing system in remote regions. A portable microwave sensing device is introduced for early-stage breast cancer detection in remote areas and the reasons behind simulating the existing portable system in a 3D environment are described.

### 2.4.2 Problems of Implementing Exiting Microwave Systems in Remote Regions

**chapter 1** illustrates that the mortality rate of breast cancer is linked to the availability of conventional BMS systems [1, 5]. The Low and Middle-income countries do not have sufficient money to diagnose breast cancer using the conventional microwave systems [72]. In Low and Middle-income countries and even remote regions of the developed countries, difficulties are experienced in implementing BMS tools due to poor communication systems. Apart from the moderate communication system, there is a significant disadvantage of the standard BMS tools. The BMS tools are enlarged in size, but the health centers of low and middle-income countries do not have enough space to install those conventional tools. This significant drawback strives to invent an innovative idea to make a difference for the low and middle-income counties, and even for the remote places of developed countries.

Due to the disadvantages of the existing breast microwave sensing (BMS) systems, an alternative approach needs to be developed for use in remote locations. This ideal BMS system should

be flexible, comfortable, and easily accessible. The system needs to be easy to move and ideally, women should be able to use the device without the help of an experienced person. To meet these needs, non-ionizing research groups of the University of Manitoba already developed two systems. One is a 2D simulated system and another one is a hardware system with antennas. The description and disadvantages for these two systems are written in the next section.

### 2.4.3 Portable Microwave Sensing Device for Remote Regions

A 2D simulated portable microwave breast cancer detection system was introduced with the advantage of rotating the device around the breast [73]. The proposed device consisted of twelve (12) solid-state sensors and a transmitting antenna corresponding to the rectangular-shaped chamber's PVC walls. Microwave signals were transmitted consisting of five (5) frequencies over the bandwidth of the transmitted antenna [74]. Point-like sensors were used and three (3) different machine learning algorithms (K-nearest Neighbors (KNN), Support Vector Machine (SVM) with a Radial Basis Function Kernel, and Neural Network) were used to detect the presence of the breast lesion [75]. A classification approach that could determine the presence of a lesion more accurately was evaluated using the datasets obtained from the system [74]. SVM classification provided 94% accuracy while the accuracy for KNN was approximately 73% [74, 75]. However, the proposed simulated portable system was a 2D simulation system and could not describe the patterns of the electromagnetic fields due to the tumors inside the simulated portable systems. The simulated system also did not describe the optimal design associated with the most appropriate number of receiving sensors and transmitters. Hence, a new 3D simulation approach should be developed to resolve these disadvantages. Additionally, the hardware set-up of the system did not try to develop. The sensitivity and specificity of the system are needed to improve with clinical approval.

To improve the described 2D simulated portable system, an experimental setup of the portable system was designed [37]. A horn antenna as the transmitter and a semi-circular sensor array consisting of thirteen (13) microstrip patch antennas were used. There was a 4 mm gap between the adjacent sensors. Voltages were estimated at the receiver side due to the different positions of the scattering object like the Al rod inside the portable system. The established hardware setup of the portable modality still faced some difficulties regarding the feasibility of the system and the experimental accuracy. A calibration process using the geometrical correlation constant should

be applied [37] to improve the experimental accuracy. For developing the experimental accuracy using the calibration process, the same portable system needs to be developed in a 3D simulation environment. The experimental portable system also did not provide the answers regarding the behaviors of the transmitted electromagnetic waves due to different positions of the scattering object inside the portable system. Analyses regarding the number of the sensors at the receiver side and the frequency range for the transmitted microwave signals were not conducted by the experimental portable system. These research questions can be answered by a 3D simulated portable system. In CST microwave software, the portable system with transmitting antenna, the imaging chamber, receiver antennas, and scatterers can be simulated in a 3D environment. In addition, the characteristics of the electromagnetic fields can be observed in CST due to different positions of the scattering material like the Al rod inside the simulated portable system.

### 2.4.4 Conclusion

This section provides the disadvantages of installing the exiting microwave breast cancer detection systems for Low- and Middle-Income countries and remote regions of developed countries. The drawbacks of the portable microwave system were investigated to improve the sensitivity and specificity of the portable system for detecting breast lesions. By investing in the disadvantages of the exiting portable system for remote regions, this section helps to determine the objectives of this thesis and answer the research questions that are included in the next section.

## 2.5 Research Questions and Objectives of this Thesis

### 2.5.1 Research Questions

The present perspective of portable microwave breast cancer detection generates the following research questions.

- What will be the design for the simulated portable system with the design of transmitter and receiver array?
- How will the point-like scatterer change the behaviors of E-field patterns inside the sensing chamber of the portable system?

- Is it possible to use an analytical approach to describe the E-field responses of the portable system due to the point-like scatterer?
- Can a simple mathematical equation be used to estimate the E-fields at the receiver array for different positions of point-like scatterer inside the sensing chamber of the portable device as the functions of frequencies and angular positions?
- Can the analytical approach be used for transfer learning in the future?

### 2.5.2 Objectives of this Thesis

The main objective of this thesis is to interpret the behaviors of the electric fields (E-fields) due to the presence of a point-like scatterer and evaluate an analytical approach to describe the E-fields.

This thesis unveils the research questions for the portable microwave detection system:

- the suitable design of the portable sensing system with transmitter and receiver array are included in **Chapter 3** for the simulation.
- the behaviors of the E-fields due to the presence of a point-like scatterer are described in **Chapter 4**.
- the analytical approach to explain the relative field strength and agreement with the simulation results are narrated in **Chapter 5**.
- the usage of the derived mathematical equation to estimate the E-fields at the receiver array for different positions of the point-like scatterer inside the sensing chamber of the portable device is demonstrated in **Chapeter 5**.
- the application of the evaluated mathematical equation for transfer learning is presented in **Chapter 5**.

# Chapter 3

# Simulated Portable Microwave Device

This chapter describes the microwave breast cancer detection device which was simulated using CST Microwave Studio [76]. The design procedure of the horn antenna is described. This chapter also compares the characteristics of the simulated horn antenna to the experimental measurements of the horn antenna taken in the laboratory.

## 3.1 Introduction of Simulated Portable Microwave Device

A portable microwave breast cancer detection system was designed to analyze the electric fields present in the device under different conditions and to provide data for deriving a mathematical model of electric field patterns. This model is intended to help in describing the relative changes in the electric fields (E-fields) with the insertion of a point-like scatterer (intended to simulate a small tumor) and generating data for transfer learning purposes. The portable system was designed using CST Microwave Studio software [76]. The simulated system consisted of 3 major parts: a transmitter, a sensing chamber, and a detector as represented in Fig. 3.1. A horn antenna was used as the transmitter. Instead of designing several independent receiver antennas, a receiver array was used to observe the electric fields' behaviors at different points of the receiver array.

### 3.1.1 Transmitter - Horn Antenna

The horn antenna was initially designed in Antenna Magus software [77] to replicate the performance of the LB-20200 Broadband Horn Antenna [78] which was a tapered ridge antenna operating over 2-20 GHz. Table 4.1 gives the technical specifications of the LB20200 Antenna, and the design of the antenna is illustrated in Fig. 3.2. After obtaining the desired performance, the

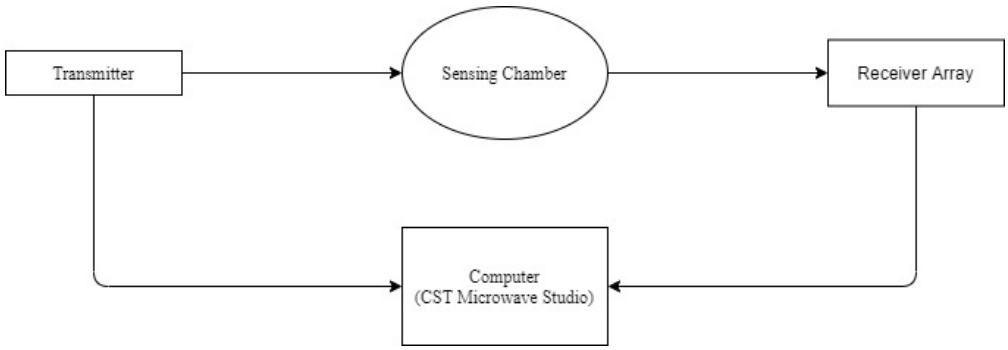


Figure 3.1: Block diagram of the simulated portable system.

antenna was imported to the CST Microwave software for further simulation and analysis. The gain, reflection coefficient (S11), and Voltage Standing Wave Ratio (VSWR) of the horn antenna were calculated and were compared with experimental measurements.

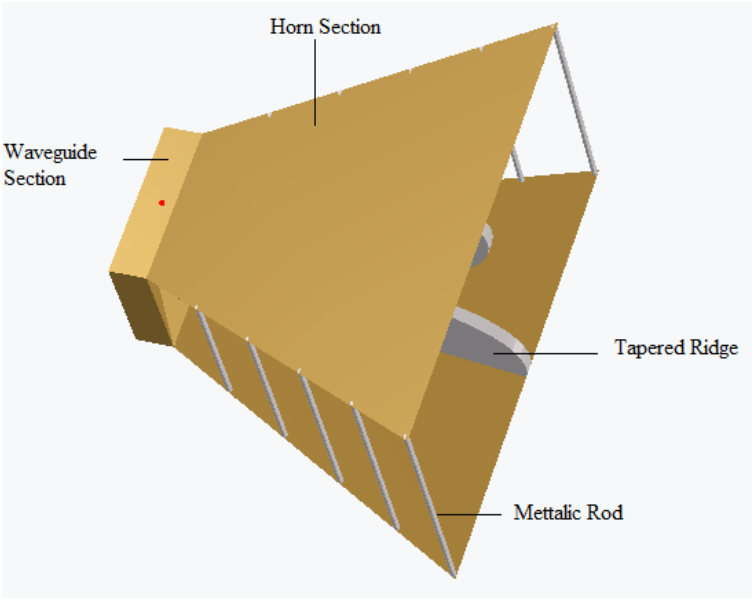


Figure 3.2: Horn Antenna.

### 3.1.2 Sensing Chamber

The sensing chamber was located between the transmitter and the receiver array. The breast was positioned in the chamber, a point-like scattering object could be placed in the chamber to evaluate the system. The geometry of the sensing chamber is shown in Fig. 3.3. Coordinate axes (X-axis and Y-axis) were used to identify different positions of the scatterer. The central (0,0) point of the chamber was positioned 11 cm away from the transmitter so that 3dB beamwidth of the transmitted

signal enabled to illuminate a 15 cm diameter breast over 2-8 GHz bandwidth and 9 cm away from the mid-point of the receiver array. The radius of the chamber was 15 cm. A breast of any radius less than 15 cm (approximately equal to 44G cup) was positioned inside the chamber for detecting breast lesions.

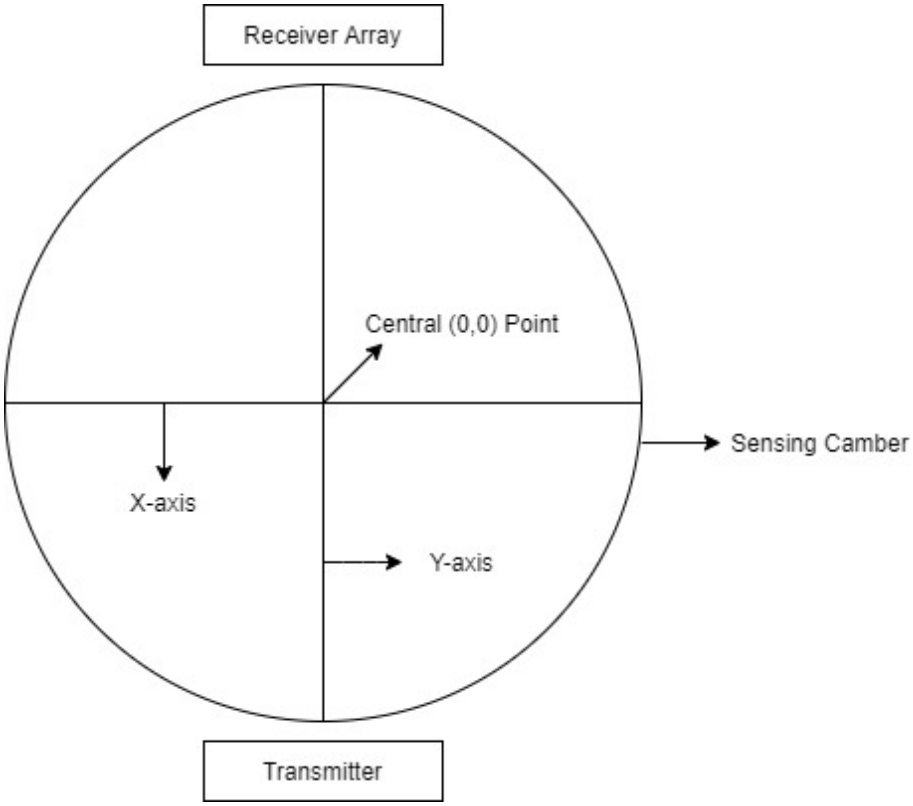


Figure 3.3: Sensing chamber.

### 3.1.3 Receiver Array

The receiver array of the portable system consisted of 37 receiver points. To perceive the behaviors of the E-fields at different points on the receiver array, the half-circle containing the receiver array had a radius of 15 cm symmetrically positioned around the axis shown in Fig. 3.4. 37 different points were considered on the half circle to observe the E-fields. To interpret the positions of 37 receiver points easily, 37 receiver points were represented as 37 different angles with respect to the y-axis (x=0). The 1st and 37th points of the receiver array occur at -90° and 90° respectively. The 19th number receiver point was generated 0° with the central (0,0) point.

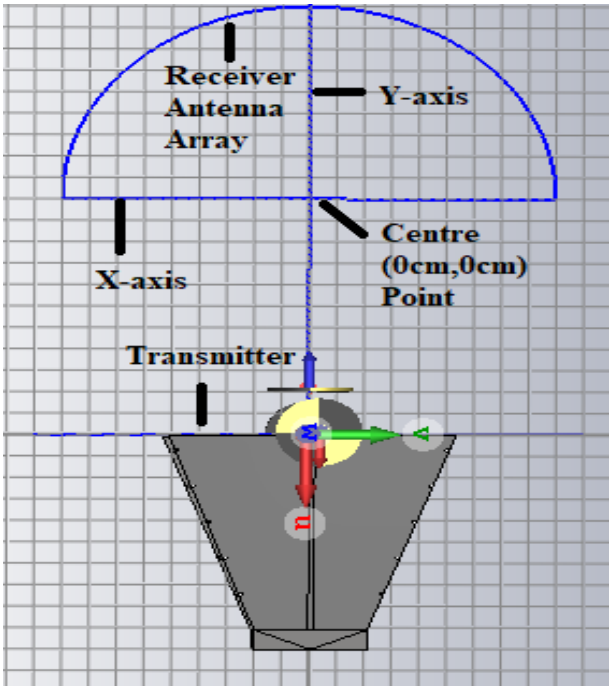


Figure 3.4: The simulated portable microwave system.

## 3.2 Methodology for Designing Horn Antenna in the CST Microwave Studio

The horn antenna was designed for operating from 2 GHz to 20 GHz. Low-frequency signals provided the potential for higher penetration, which increased the signal-to-noise ratio (SNR) for larger breasts [79]. However, the antenna size increased at low frequency which was not ideal for the portable system. While designing the antenna for higher frequencies reduced the antenna size, the penetration depth decreased and the optimal range of operating frequency was found to range from 2 to 8 GHz. The configuration of the horn antenna design is given in Table 4.1. The overall length of the horn antenna was 99 mm with a 90 mm flare length and 9 mm waveguide length to obtain the necessary bandwidth. The horn antenna contained four sections - a horn section, a waveguide section, a feed section, and the ridges. The top and side views of the horn antenna are shown in Fig. 3.5 having an axial length ($L_f$) of 90 mm, an aperture width ($W_a$) of 104 mm, an aperture height ($H_a$) of 70 mm, a waveguide height ($H_g$) of 40 mm, and a waveguide width ($W_g$) of 41 mm.

The horn section of the designed antenna was connected to a rectangular waveguide. The

| Name of Parameters | Used Values in mm |
|---|---|
| Flare Length | 90 |
| Aperture Height | 104 |
| Aperture Width | 78 |
| Waveguide Height | 49 |
| Waveguide Width | 41 |
| Ridge Width | 1.9 |
| Ridge Spacing | 0.48 |
| Coaxial Inner Diameter | 0.52 |
| Cavity Height | 11.5 |

Table 3.1: Configuration of the designed horn antenna.

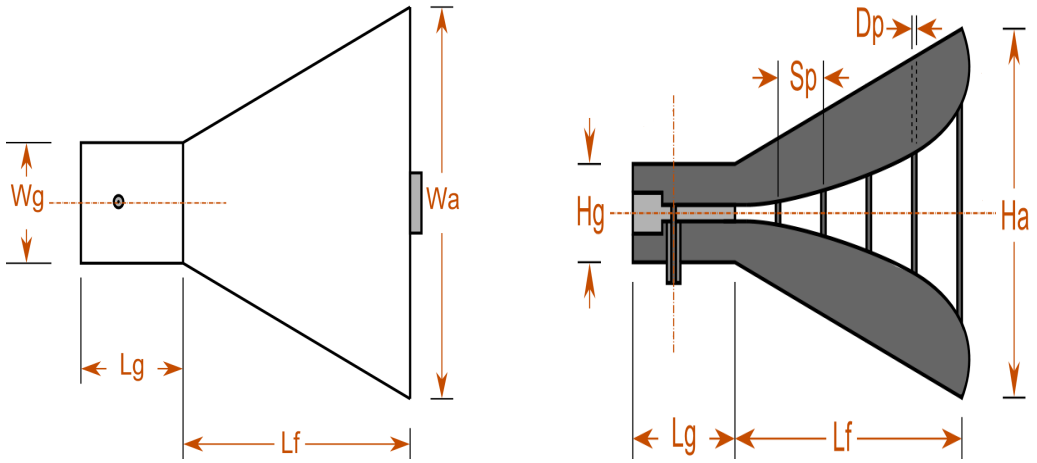


(a) (b)

Figure 3.5: (a) Top view of horn antenna and (b) Side view of horn antenna.

antenna had also a rectangular back cavity. The waveguide closed at the backside to decrease the return loss and direct the radiation in the forward direction [80]. While the dimension of the back cavity played a vital role in the return loss and radiation pattern of the antenna, no analytical approach had been found to design the back cavity [81]. Instead, the dimensions of the back cavity for the proposed antenna were empirically determined by changing the parameters of the back cavity until the desired return loss was obtained. For the desired return loss, the dimension of the back cavity had a width of 22.77 mm, a length of 7.00 mm, and a height of 11.50 mm. Five flare walls provide the transmission from the waveguide section to the free space. The flare walls had a negligible effect on the antenna's performance at high frequencies because of the high electrical

energy concentration between the ridges but had some adverse impacts at low frequencies [81]. The side flares contained metallic rods and a 0.48 mm gap was used between the ridges to overcome the effects at frequencies below 4 GHz [81]. The impedance of the antenna converted from 50 ohms at the feeding point to 377 ohms in the air (free space).

There were numerous ridge profiles used for the horn antenna design and the ridge profiles include exponential, sinusoidal, and binomial form [81]. The exponential curve improved the impedance matching between the waveguide section and the free space. If a linear part was added to the exponential part, the Voltage Standing Wave Ratio (VSWR) was low at low frequencies. In this work, a Bezier curve shown in Fig. 3.6 was used to provide the necessary impedance matching control instead of an exponential curve.

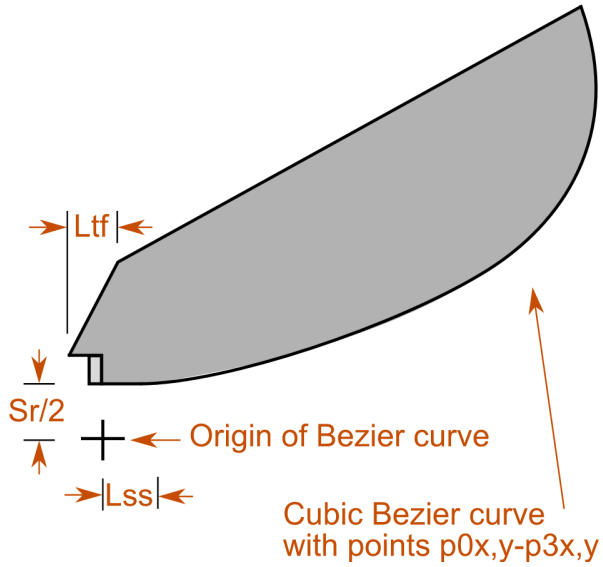


Figure 3.6: Bezier curve of horn antenna.

The feed coupled the energy through the upper ridge into the gap and provided the pathway to connect the conductor to the upper and lower ridges. The inner configuration of the horn antenna is displayed in Fig. 3.7. The following impedance matching equation was used to match the impedance of the feed with the aperture of the antenna represented in (3.1) and (3.2) [82].

$$z(k) = z_0 e^{kz} \tag{3.1}$$

where z is the distance from the waveguide aperture, L is the axial length of the flare section. The

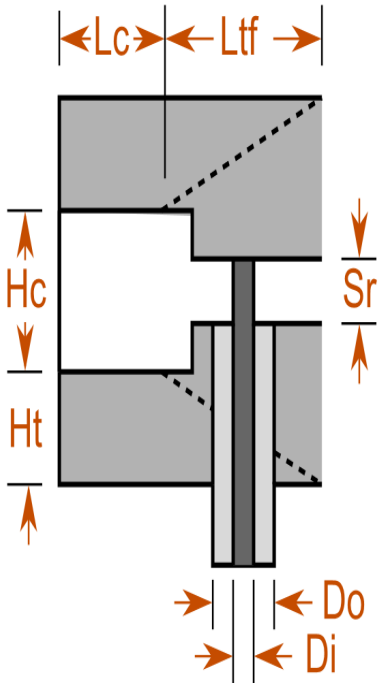


Figure 3.7: Inner configuration of horn antenna.

value of k was determined by the following equation.

$$k = \frac{1}{L} \ln \frac{z_L}{z_0} \tag{3.2}$$

Here, $z_L$ and $z_0$ are the characteristic impedances of the double-ridged rectangular waveguide and the free space, respectively.

## 3.3 Result and Discussion

### 3.3.1 Reasons behind the Use of Horn Antenna as a Transmitter

Antennas for use in breast imaging must have a beam pattern sufficiently wide to encompass the entire breast while having sufficient directivity to detect the energy scattered by the tumors [79]. The 3dB beamwidth of this design enabled a 15 cm diameter breast (roughly equivalent to a 44E cup) to be illuminated from 11 cm away over the 2 - 8 GHz bandwidth at which the system normally operated. The directional radiation pattern and wide impedance bandwidth were considered as other characteristics for using this antenna design in the breast cancer detection system.

### 3.3.2 Comparison between the Simulated Horn Antenna and the Horn Antenna Used in Laboratory

The simulation of horn antenna in CST Microwave Studio is shown in Fig. 3.8. The recorded reflection coefficient from the simulated horn antenna was compared with the measured reflection coefficient from the horn antenna using the Vector Network Analyzer (VNA) and is presented in Fig. 3.9. A bandwidth agreement of 90% at -10 dB between the simulated and measured reflection coefficients was obtained. The resonant frequency was at 4.3 GHz frequency for both simulated and measured reflection coefficients. In agreement with the published data for the LB-20200 antenna, the VSWR of the simulated antenna shown in Fig. 3.10 was less than 2 over the 2 GHz to 8 GHz bandwidth. The radiation patterns between the simulation and the measurement were compared and agreed to within 96%. The return losses were also compared between the simulated and the measured values. In Fig. 3.11, the antenna gains of the simulated and laboratory horn antennas were compared.

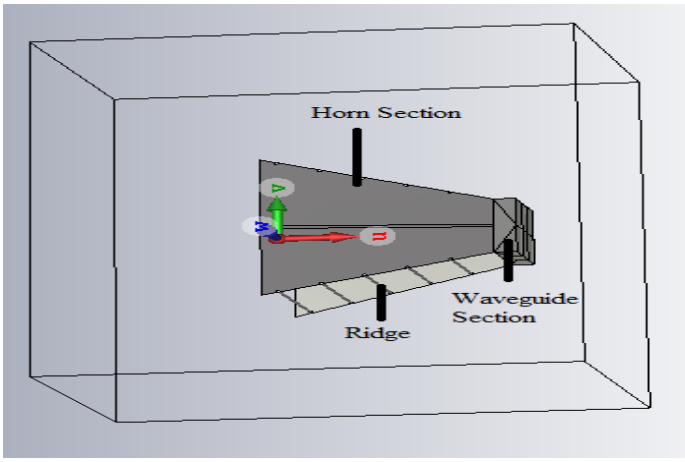


Figure 3.8: The simulated horn antenna.

As illustrated in Fig. 3.12, two equivalent horn antennas positioned facing each other and separated by 200 m were simulated in CST Microwave Studio, and likewise, two LB-20200 horn antennas were similarly positioned experimentally. The open space reflection coefficients and return losses were simulated and measured.

As shown in Fig. 3.13, a 2 mm copper plate and polycarbonate plate of 2 mm thickness and 200 mm diameter were independently placed at an equal distance between the two horn antennas. The

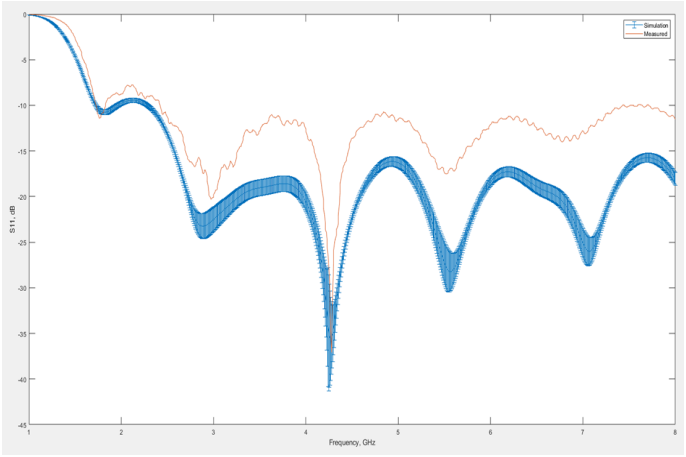


Figure 3.9: Reflection coefficient (S11) of the simulated horn antenna and measured reflection coefficient from lab horn antenna.

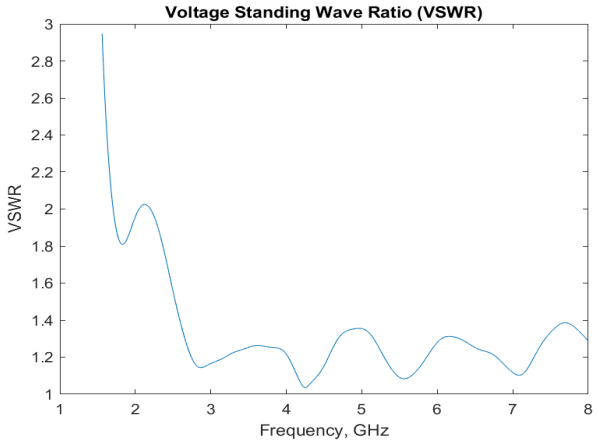


Figure 3.10: VSWR of the simulated horn antenna.

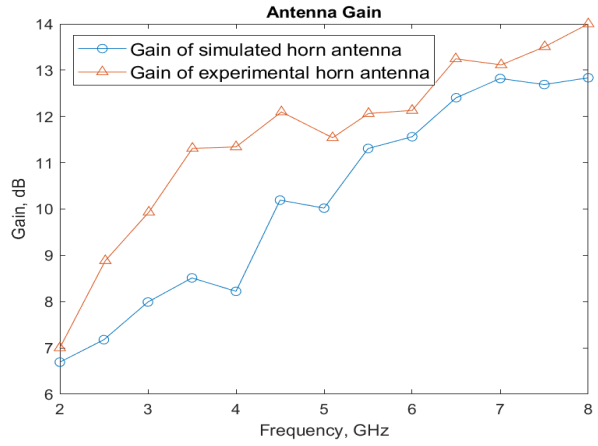


Figure 3.11: Antenna gain.

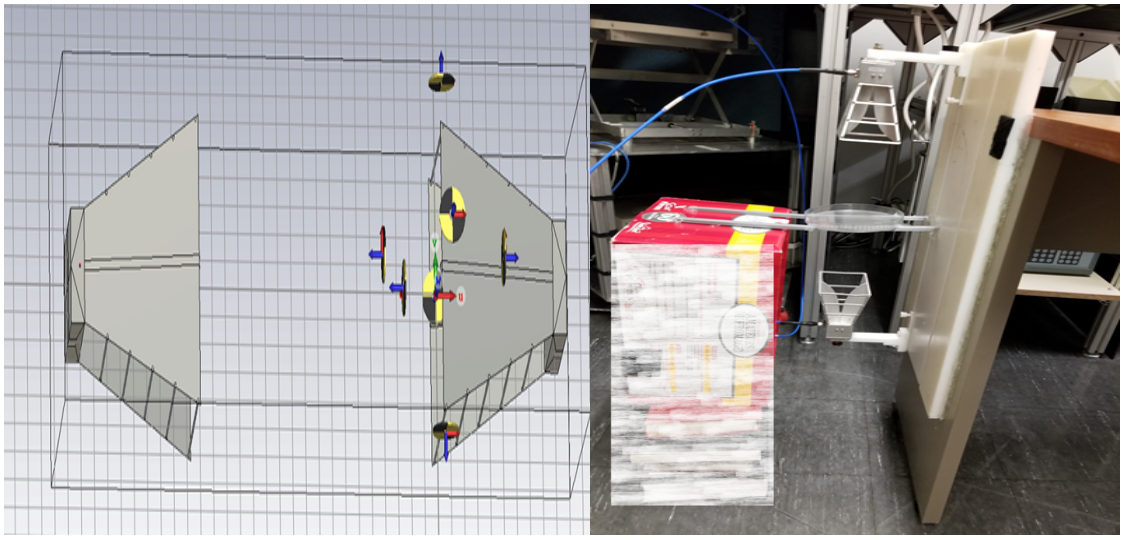

(a) (b)

Figure 3.12: (a) Simulation setup and (b) Experimental setup.

simulated and measured transmission losses (S11, S12, S21, and S22) were compared for these described conditions. The simulated and measured transmission losses were displayed in Fig. 3.14 only for the polycarbonate plate conditions. The accomplished desirable agreements were observed for the use of the horn antenna because of future analysis such as the future design of the portable system with the horn antenna in CST Microwave Studio.

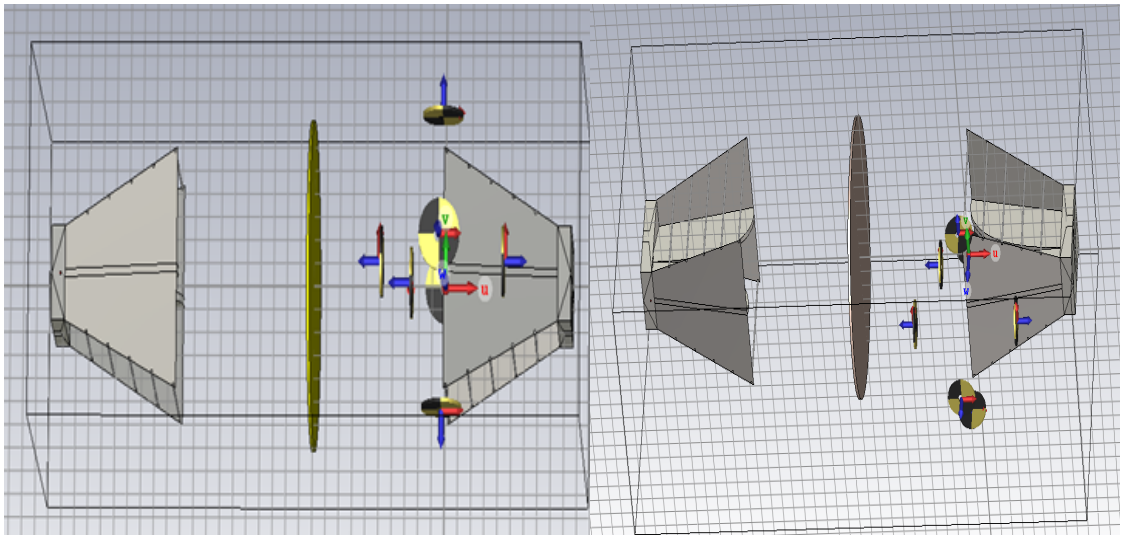

(a) (b)

Figure 3.13: Transmission through (a) copper plate (b)polycarbonate plate.

Theoretically calculated E-fields and simulated E-fields were compared using Equations (3.3)

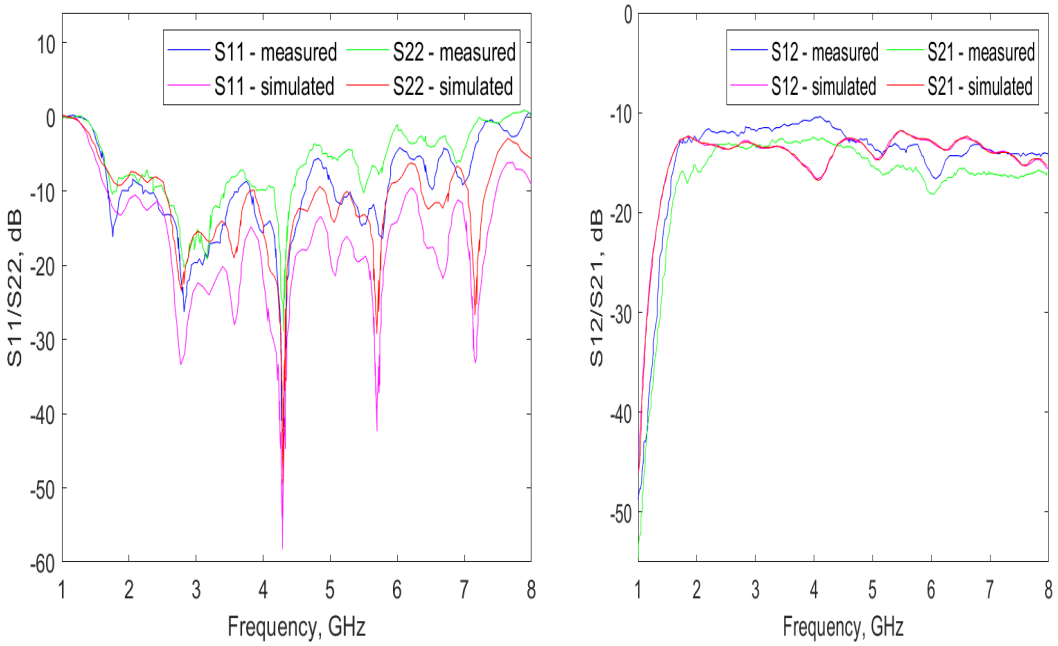


(a) (b)

Figure 3.14: S-parameters - (a) S11/S22 and (b) S12/S21 when transmission occurred through polycarbonate plate.

and (3.4) for several frequencies.

$$P_{\mathrm{r}} = \frac{E^2 \lambda^2 G_{\mathrm{r}}}{480\pi^2} \tag{3.3}$$

$$\frac{P_{\mathrm{r}}}{P_{\mathrm{t}}} = D_{\mathrm{t}} D_{\mathrm{r}} (\frac{\lambda}{4\pi d})^2 \tag{3.4}$$

where $P_t$ and $P_r$ are the power of the transmitter and receiver respectively. $D_t$ and $D_r$ are the gain of the transmitter and receiver respectively. d is the distance between transmitter and receiver and d was assumed as 1 mm.

For 5 GHz, the theoretically calculated E-field was obtained at 25.42 V/m, while CST Microwave Studio calculated a value of 24.6 V/m. 28.44 V/m of E-field was evaluated theoretically and 26.3 V/m was accomplished from CST Microwave Studio for 6 GHz. The difference of E-field was 2 V/m between theoretical analysis and simulation. Hence, the E-field with the standard error of 2 V/m was considered for this study.

## 3.4 Conclusion

This chapter describes a simulated portable breast cancer detection system. The horn antenna was designed using the same characteristics as the horn antenna used for the experimental work in the laboratory. Various characteristics (reflection coefficient, transmission coefficient, gain, and VSWR) of the simulated horn antenna were compared with the horn antenna used in the laboratory under different experimental conditions. To maintain simplicity, the simulated system used 37 points on the receiver array (instead of designing independent antennas as receivers) to measure the propagated E-fields from the transmitted horn antenna.

# Chapter 4

# Analysis for a Point-like Scatterer

This chapter describes the behavior of the detected electric field (E-fields) due to a point-like scatterer inside the portable microwave system. The changes of E-fields detected by the receiver array for different positions of the scatterer changed inside the sensing chamber were simulated using CST Microwave Studio. This chapter also investigates the conditions required to identify the changes of the detected E-fields due to the changes in the positions of the scatterer.

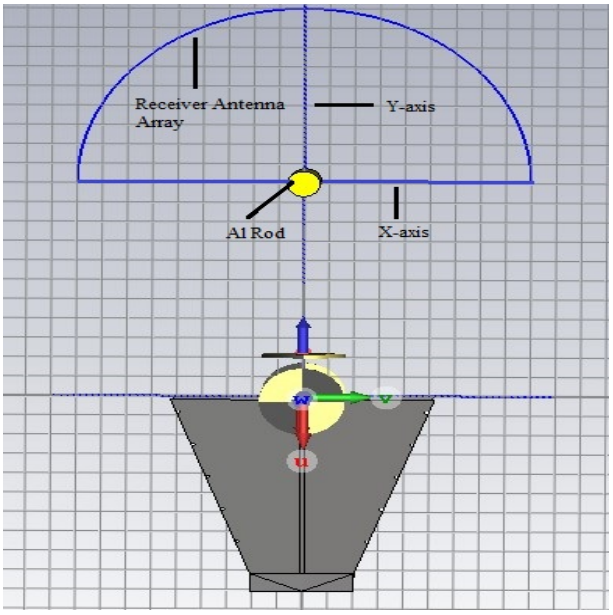


Figure 4.1: Portable microwave system with Al rod at (0,0) point.

## 4.1 Introduction - Simulation for a Point-like Scatterer

An aluminum (Al) rod was used as a point-like scatterer to investigate the response of the portable system. The diameter of the Al rod was 6.45 mm and the height of the Al rod was 170 mm. The Al

rod was situated at different positions of the sensing chamber, such as shown in Fig. 4.1. For each Al rod position, the portable system was simulated in CST Microwave Studio for 15 frequencies from 1 GHz to 8 GHz and the E-fields were estimated for those 15 frequencies. The E-fields were also simulated over the frequency range with no Al rod in the chamber (open-space condition). This open-space condition was considered as the reference.

## 4.2 Methodology

For simplification of the positions of Al rod in the sensing chamber, X-axis and Y-axis were divided into positive and negative axes. If the right side of X-axis was assumed as positive X-axis and the left side of X-axis was assumed as negative X-axis. Y-axis from the central (0cm,0cm) point to the midpoint of the receiver array was considered as positive Y-axis and Y-axis from transmitter to the central (0cm, 0cm) point was considered as negative Y-axis. Radius of the sensing chamber for Al rod was taken as 6cm. Al rod was positioned at different points inside the sensing chamber within this considered 6cm radius.

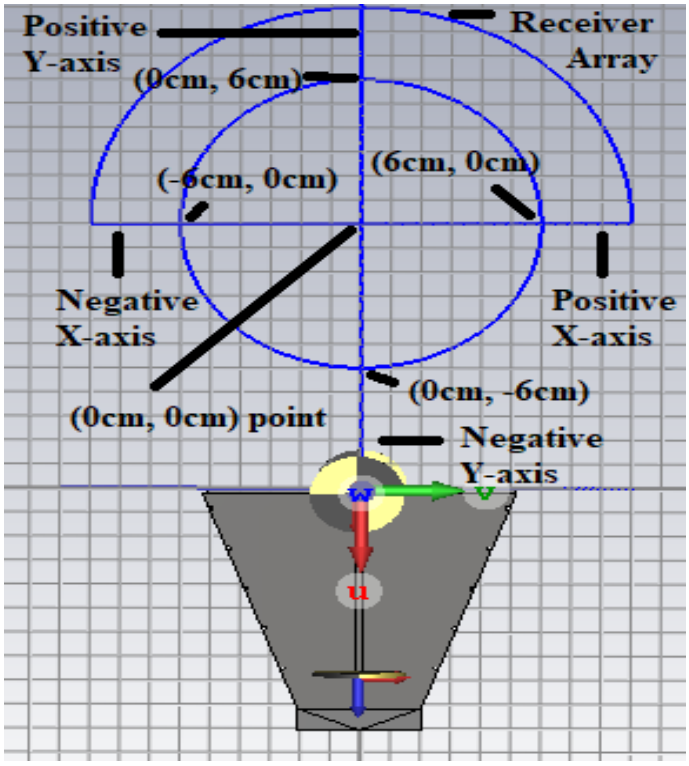


Figure 4.2: Sensing chamber inside the simulated portable device.

For each Al rod position, the ratio of the E-field intensity to the open-space for each frequency was evaluated. As an example, Fig. 4.3 shows the ratios of E-field intensities for 3 different frequencies and 3 different positions of the Al rod.

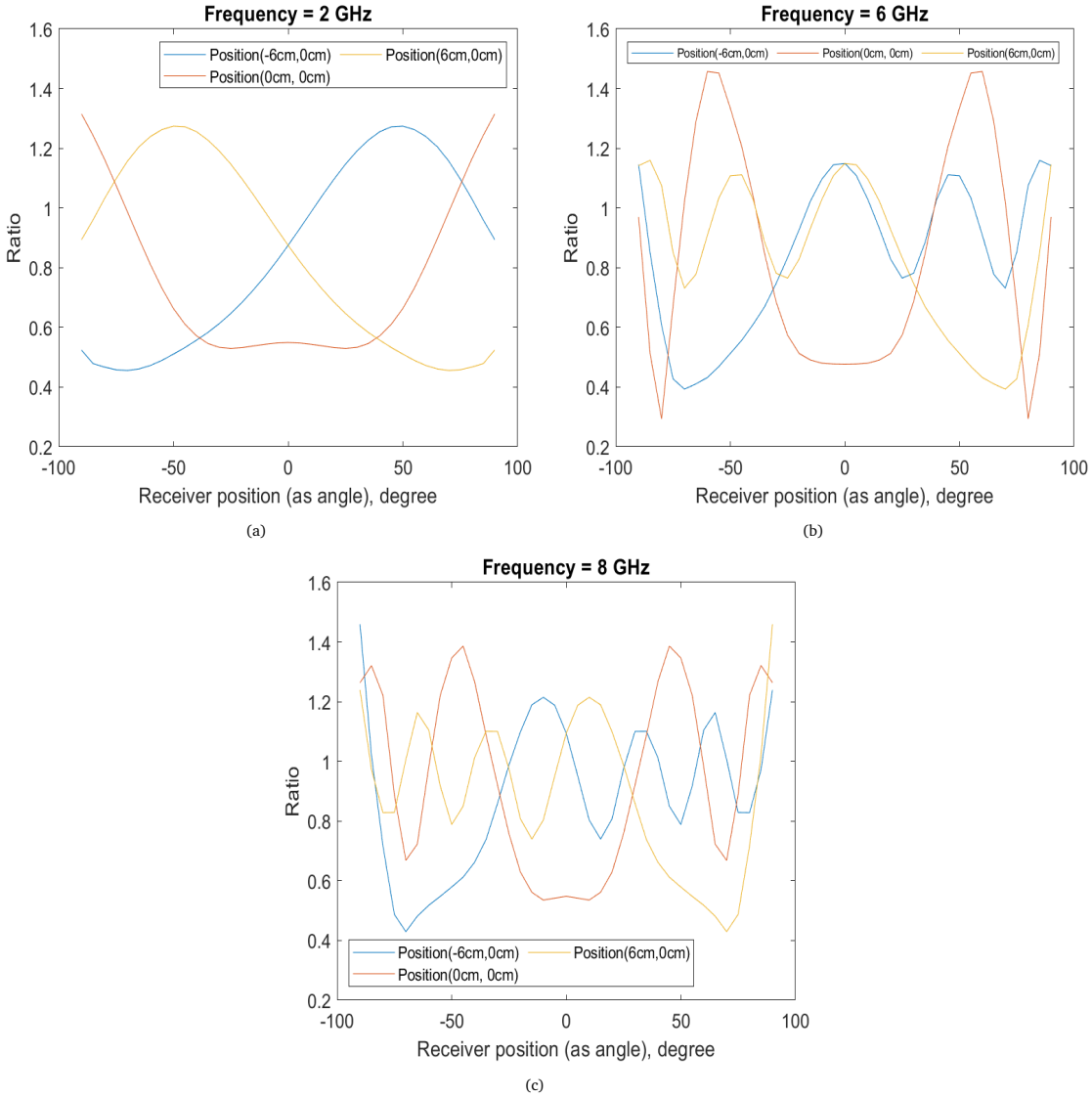


Figure 4.3: Ratios of E-field intensities for 3 different positions of Al rod at (a)Frequency = 2 GHz,(b) Frequency = 6 GHz and (c) Frequency = 8 GHz.

The averaged E-field intensity was also obtained from the individual E-field intensities at 1 GHz to 8 GHz for the open space condition and each Al rod position. The ratio of the E-field intensity was calculated for each Al rod's position using the division of the averaged E-field intensity for each Al rod position by the averaged E-field intensity of the open-space condition. The averaged ratios of E-field intensities for rod positions along the X-axis and Y-axis are displayed in Fig. 4.4 and

the averaged ratios of E-field intensities for rod positions on y = -2cm and y= 2cm are shown in Fig. 4.5.

## 4.3 Result and Discussion

The E-fields at the receiver antenna array followed the constructive and destructive interference properties of the transmitted and scattered signals for different Al rod positions. As a result of the symmetry of the system, when the Al rod was at the (-6 cm, 0 cm) position, the ratio of E-fields observed by the 1st receiver point was the same as the ratio of E-field intensities obtained from the 37th number receiver point at 2 GHz, 6 GHz, and 8 GHz. The ratio of E-field intensities for 1st and 37th number receiver points are the same for the Al rod at the (0 cm, 0 cm) position for each frequency. Fig. 4.3 illustrates the symmetrical behavior of the ratio of the E-field intensities detected by the receiver array due to the Al rod situated at opposite sides of the coordinate axes when y=0 and the same X-axis.

Table 4.1: Al rod's behaviors along the X-axis (y=0cm) from Fig. 4.4

| Positions of Al rod | Maximum peak's conditions at left side | | Maximum peak's conditions at right side | |
|---|---|---|---|---|
| | Receiver Positions | Ratio of E-field Intensities | Receiver Positions | Ratio of E-field Intensi |
| (-4cm, 0cm) | -90° ± 5° | 1.33 ± 0.22 | 20° ± 5° | 1.164 ± 0.22 |
| (-2cm, 0cm) | -75° ± 5° | 1.28 ± 0.22 | 40° ± 5° | 1.21 ± 0.22 |
| (0cm, 0cm) | -55° ± 5° | 1.24 ± 0.22 | 55° ± 5° | 1.24 ± 0.22 |
| (2cm, 0cm) | -40° ± 5° | 1.21 ± 0.22 | 75° ± 5° | 1.28 ± 0.22 |
| (3cm, 0cm) | -30° ± 5° | 1.18 ± 0.22 | 85° ± 5° | 1.28 ± 0.22 |
| (4cm, 0cm) | -20° ± 5° | 1.16 ± 0.22 | 90° ± 5° | 1.33 ± 0.22 |
| (5cm, 0cm) | -10° ± 5° | 1.15 ± 0.22 | more than 90° | unknown |

It is also observed from Fig. 4.4 and Fig. 4.5 that the peaks of the averaged ratios shifted in angle as the Al rod's position shifted along the X-axis (y = 0cm), y = -2cm, and y = 2cm. The received E-fields characteristics are displayed in Table 5.1 for the change of Al rod's position along the X-axis (y=0cm). For movements on the Y-axis (x = 0cm), the peaks moved to larger angles as the Al rod shifted from the positive Y-axis (closet to the receiver) to the negative Y-axis (closet to the transmitter). The widths of the trough caused by the attenuation of the rod at the center of the array narrow as the rod moves in the positive Y-direction taking it closer to the receiver antennas.

The ratios of E-field intensities' behaviors due to the change of Al rod's positions along the Y-axis are shown in Table 5.2.

Table 4.2: Al rod's behaviors along the Y-axis (x=0cm) from Fig. 4.4

| Positions of Al rod | Widths | Ratio of E-field Intensities | Receiver positions at maximum peaks | |
|---|---|---|---|---|
| | | | Left side | Right side |
| (0cm, -4cm) | 160 $\pm$ 5 | 1.30 $\pm$ 0.22 | -80° $\pm$ 5° | 80° $\pm$ 5° |
| (0cm, -2cm) | 130 $\pm$ 5 | 1.28 $\pm$ 0.22 | -65° $\pm$ 5° | 65° $\pm$ 5° |
| (0cm, 0cm) | 110 $\pm$ 5 | 1.24 $\pm$ 0.22 | -55° $\pm$ 5° | 55° $\pm$ 5° |
| (0cm, 2cm) | 100 $\pm$ 5 | 1.23 $\pm$ 0.22 | -50° $\pm$ 5° | 50° $\pm$ 5° |
| (0cm, 4cm) | 80 $\pm$ 5 | 1.22 $\pm$ 0.22 | -40° $\pm$ 5° | 40° $\pm$ 5° |

Two conditions that were considered for fitting the ratio of the received E-fields at the receiver array using a mathematical equation were achieved from Fig. 4.4, Fig. 4.5, Table 5.1, and Table 5.2. Mathematical modeling of the ratios of the E-field intensities should accurately be able to represent by the following conditions.

- the maximum peak occurring points
- the width of the ratio curves

## 4.4 Conclusion

The suitability of the portable approach was described for a large number of point-like responses. The details of the received E-fields' changes as a result of inserting the Al rod at different positions in the sensing chamber were illustrated. Finally, two characteristics of the ratios of E-field intensities to the open-space conditions were evaluated that were applied to mathematical modeling for estimating the ratios of E-field intensities at the receiver side as a function of frequencies and positions of Al rod.

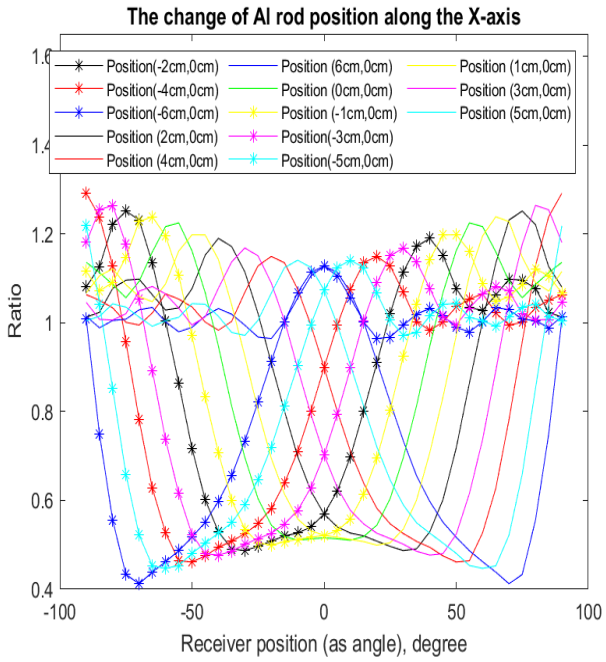


(a)

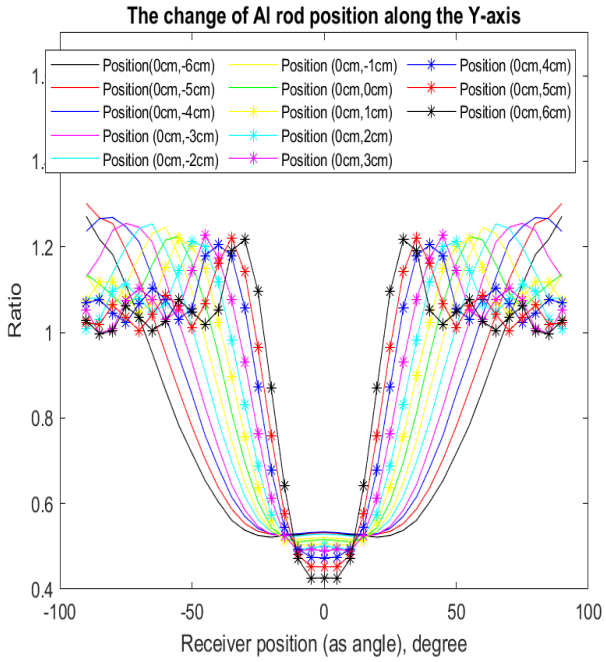


(b)

Figure 4.4: (a) The averaged ratio of E-field intensities when Al rod on the X-axis (y = 0cm) and (b) The averaged ratio of E-field intensities when Al rod on the Y-axis (x = 0cm)

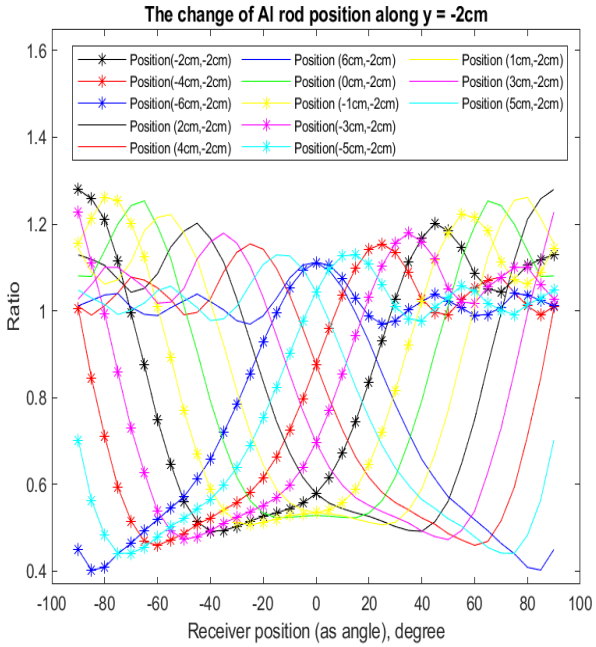


(a)

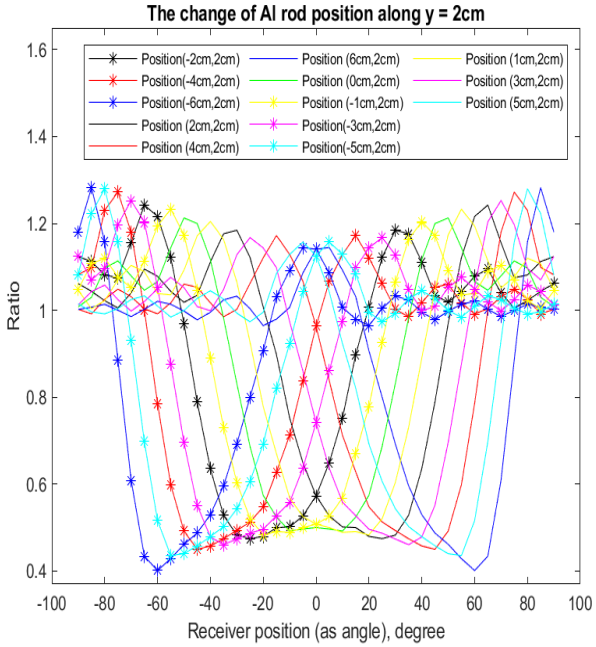


(b)

Figure 4.5: (a) The averaged ratio of E-field intensities when Al rod on y = -2cm and (b) The averaged ratio of E-field intensities when Al rod on y = 2cm

# Chapter 5

# Mathematical Modeling of the Portable Microwave Breast Cancer Detection System

This chapter provides the details of the mathematical equation that represents the ratios of the E-field intensities detected by the receiver array on account of different positions of the Al rod. The proposed mathematical equation was further modified to describe the behaviors of E-fields in a 3D situation as a function of frequencies, receiver positions, and Al rod's positions. The behaviors of different parameters of the mathematical modeling as the functions of different frequencies and positions of the Al rod were also derived.

## 5.1 Initial Mathematical Modeling

### 5.1.1 Introduction

Mathematical modeling was developed for evaluating the behaviors of the received E-fields as a function of Al rod's positions in the sensing chamber and receiver positions on the receiver array. The simulated portable microwave system consisted of a complex structure with the transmitter, receiver array, and sensing chamber. Some assumptions were taken for the simplification of the simulated system and the evaluation of the received E-fields by a mathematical equation.

### 5.1.2 Methodology

The simulated portable system was represented simply by considering some assumptions. The geometric layout of the portable system with a transmitter, the sensing chamber, and the receiver array is shown in Fig. 5.1. The distance between the transmitter and the midpoint of the receiver

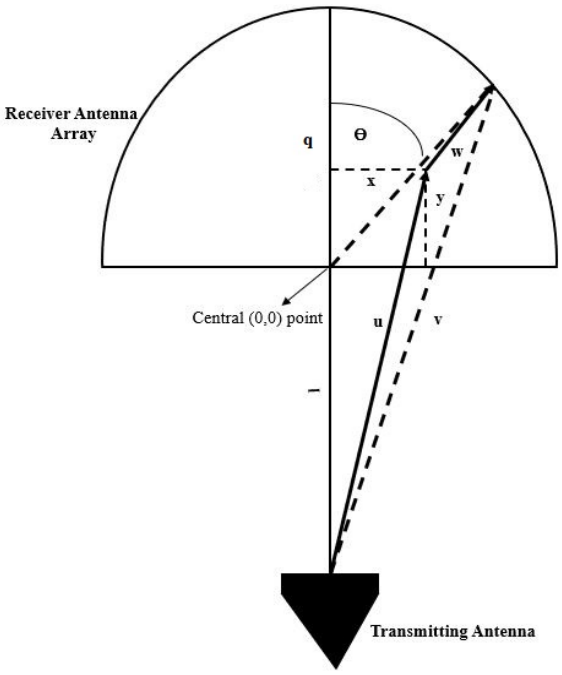


Figure 5.1: Geometrical layout of the simulated portable BMS system when Al rod is placed at (x, y) point in the considered coordinate axes.

array was 20cm. Al rod that was considered as a point-like scatterer was placed at different positions in the sensing chamber of the portable system.

For the geometrical representation of the portable system, X-axis (y=0) and Y-axis (x=0) were considered. A center (0, 0) point on the X-axis (y=0) was assumed between the transmitter and the midpoint of the receiver array. The distances from the transmitter antenna to the centre (0,0) point and from the centre (0, 0) point to the midpoint of the receiver array were l and q respectively where l = 0.11m and q = 0.09m were considered. An arbitrary (x, y) point was considered for the Al rod with respect to the centre (0, 0) point. v was the distance from the transmitter antenna to the point of measurement at the receiver array, w was the distance from the (x, y) point of the Al rod to the point of measurement at the receiver array and u was considered as the distance from the transmitter antenna to the (x, y) point of the Al rod. $\theta$ was assumed as the angles for 37 different receiver points with respect to the considered centre (0, 0) point on the X-axis.

Here,

$$|u| = \sqrt{(l+y)^2 + x^2} \text{ in m,}$$

$$|w| = \sqrt{(qcos\theta - y)^2 + (qsin\theta - x)^2} \text{ in m, and}$$

$$|v| = \sqrt{(l + qcos\theta)^2 + (qsin\theta)^2} \text{ in m.}$$

The electromagnetic waves transmitted from the transmitter antenna travel at the speed of light (c = $3 \times 10^8\ ms^{-1}$) in the open space with the synchronized propagation of electric and magnetic fields in the $\hat{z}$ direction. The electric field ($E$) of the propagated electromagnetic wave ($Vm^{-1}$) and power (S) per unit area ($Wm^{-2}$) can be written as Equations (5.1) and (5.2) respectively where

U is the amplitude of the electromagnetic wave in m,

$\phi$ is the phase shift,

f is the frequency, and

t is the time in s.

$$E = Ucos(\frac{2\pi}{c}fz - 2\pi ft + \phi) \tag{5.1}$$

$$S = \epsilon_0 cE^2 = \epsilon_0 c(Ucos(\frac{2\pi}{c}fz - 2\pi ft + \phi))^2 \tag{5.2}$$

Intensity ($I$) in $Wm^{-2}$ that is the average power per unit area for a continuous sinusoidal electromagnetic wave can be described by Equation (5.3).

$$I =< S >=< \epsilon_0 cE^2 >= \frac{1}{2}\epsilon_0 cU^2 \tag{5.3}$$

Source power ($P_s$) can be written as Equation (5.4) from Equations (5.2) and (5.3).

$$P_s = 4\pi r^2 < S >= 2\pi\epsilon_0 cr^2U^2 \tag{5.4}$$

The amplitude ($U$) of the electric field can be written as Equation (5.5).

$$U = \frac{P_s}{2\pi\epsilon_0 cr} \tag{5.5}$$

The open-space electric field ($E_{oS}$) at the receiver array can be written as Equation (5.6).

$$E_{oS} = \frac{P_s}{2\pi\epsilon_0 cv}cos(\frac{2\pi}{c}fv - 2\pi ft + \phi) \tag{5.6}$$

Open-space intensity ($I_{\text{oS}}$) at the receiver array can be shown in Equation (5.8).

$$I_{\text{oS}} =< \epsilon_0 c {E_{\text{oS}}}^2 > \tag{5.7}$$

$$or, I_{\text{oS}} = \frac{{P_{\text{s}}}^2}{8\epsilon_0 c\pi^2 v^2} \tag{5.8}$$

When the transmitter transmitted the electromagnetic signals, power created at Al rod's position (x, y) can be represented as Equation (5.9) where R is the effective radar cross-section of Al rod in $m^2$.

$$P_{\text{r}} = \frac{P_{\text{s}} R}{4\pi u^2} \tag{5.9}$$

The electric field at the receiver array due to the presence of Al rod can be displayed as Equation (5.10).

$$E_{\text{rS}} = \frac{P_{\text{s}} R}{8\pi^2 \epsilon_0 c w u^2} cos(\frac{2\pi}{c} fw - 2\pi ft + \psi) \tag{5.10}$$

For this simulated microwave breast cancer detection device, the receiving antenna array received two electric fields (E-fields) for the open space condition and the presence of the Al rod in the sensing chamber. These two electric fields ($E_{\text{oS}}$ and $E_{\text{rS}}$) received by the receiver array of the simulated device should be summed. The summation of these received electric fields ($E$) at the receiver array can be written as Equation (5.12).

$$E = E_{\text{oS}} + E_{\text{rS}} \tag{5.11}$$

$$or, E = \frac{P_{\text{s}}}{2\pi\epsilon_0 cv} cos(\frac{2\pi}{c} fv - 2\pi ft + \phi) + \frac{P_{\text{s}} R}{8\pi^2 \epsilon_0 c w u^2} cos(\frac{2\pi}{c} fw - 2\pi ft + \psi) \tag{5.12}$$

After that, the Intensity ($I$) of the total electric fields ($E$) at the receiver array for the presence of the Al rod in (x, y) point in the coordinates is illustrated in Equation (5.15).

$$I =< \epsilon_0 c E^2 > \tag{5.13}$$

$$or, I = \epsilon_0 c \lim_{T\to\infty} \int_t^{T+t} \frac{(\frac{P_s}{2\pi\epsilon_0 cv}(cos(\frac{2\pi}{c}fv - 2\pi ft' + \phi) + \frac{P_s R}{8\pi^2\epsilon_0 cwu^2}cos(\frac{2\pi}{c}fw - 2\pi ft' + \psi)))^2}{T} dt' \tag{5.14}$$

$$or, I = \frac{{P_s}^2}{8\epsilon_0\pi^2 cv^2}(1 + \frac{R^2v^2}{16\pi^2w^2u^4} + \frac{Rv}{2\pi wu^2}cos(\frac{2\pi}{c}fv - \frac{2\pi}{c}fw + \phi - \psi)) \tag{5.15}$$

Finally, the ratio of intensity at the receiver array due to the Al rod in (x, y) point in the coordinates with respect to the intensity ($I_{oS}$) at the receiver array for the open-space condition can be written as (5.18) where $\Lambda = \frac{uw}{v}$.

$$Ratio = \frac{I}{I_{OS}} \tag{5.16}$$

$$or, Ratio = 1 + (\frac{vR}{2\times 2\pi uw})^2 + \frac{vR}{2\pi uw}cos(\frac{2\pi}{c}fv - \frac{2\pi}{c}fw + \phi - \psi) \tag{5.17}$$

$$or, Ratio = 1 + (\frac{c_1}{2\times u\Lambda})^2 + \frac{c_1}{u\Lambda}cos(c_2(v-w) + c_3) \tag{5.18}$$

Consider,

$$c_1 = \frac{R}{2\pi}\ (m^2)$$
$$c_2 = \frac{2\pi f}{c}\ (radian(m^{-1})), \text{ and}$$
$$c_3 = \phi - \psi\ (radian)$$

When the cosine term is equal to -1, the ratio can be estimated as (5.19).

$$Ratio = 1 + (\frac{c_1}{2u\Lambda})^2 - \frac{c_1}{u\Lambda} \tag{5.19}$$

If the cosine term is equal to 0, the ratio can be written as (5.20).

$$Ratio = 1 + (\frac{c_1}{2u\Lambda})^2 \tag{5.20}$$

Again, when the cosine term is equal to 1, the ratio can be derived as (5.21)

$$Ratio = 1 + (\frac{c_1}{2u\Lambda})^2 + \frac{c_1}{u\Lambda} \tag{5.21}$$

### 5.1.3 Results and Discussion

For each Al rod position, the magnitude of E-field for a particular frequency was divided by the open-space E-field's magnitude for that frequency. By doing so, the ratios of E-field intensities for 15 different frequencies were calculated for each Al rod's position. The ratio curves of the magnitudes of the E-fields for each Al rod's position were fitted using (5.18) for each frequency. When the ratio curves were fitted using (5.18), 2 (two) following conditions were considered for understanding the behaviors of the derived (5.18) equation.

- Parameter $c_3 = 2\pi$ or $180^\circ$
- Parameter $c_1 = c_4$ only for 3rd part of (5.18) that makes the equation (5.18) as the following equation (5.22).

$$Ratio = 1 + (\frac{c_1}{2u\Lambda})^2 + \frac{c_4}{u\Lambda} cos(c_2(v - w) + c_3) \tag{5.22}$$

The ratio curves were fitted for the Al rod's positions along the considered X-axis (y=0) and Y-axis (x=0) individually. The peaks of the fitted curves for different Al rod's positions and different frequencies occurred at the same receiver positions just like the ratio curves obtained from the simulation for the same Al rod's positions and frequencies. One thing that should be noted is that there were no peaks for some frequencies. For those conditions, the minimum values and the widths of the ratio curves were considered as the references for fitting the ratio curves using (5.18).

When the previously described conditions were assumed, the R-squared values were obtained around $99\% \pm 0.99\%$ for all fittings. The fitted curves obtained from (5.18) and the simulated data are represented in Fig. 5.2 for 3 different frequencies and Al rod's positions.

The values of the parameters $c_1$, $c_2$, and $c_4$ were evaluated for each Al rod's position at each simulated frequency represented in Fig. 5.3. It is observed from Fig. 5.3a and Fig. 5.3c that the values of $c_1$ and $c_4$ were minimum and around zero. It is also noticed from the fittings for different

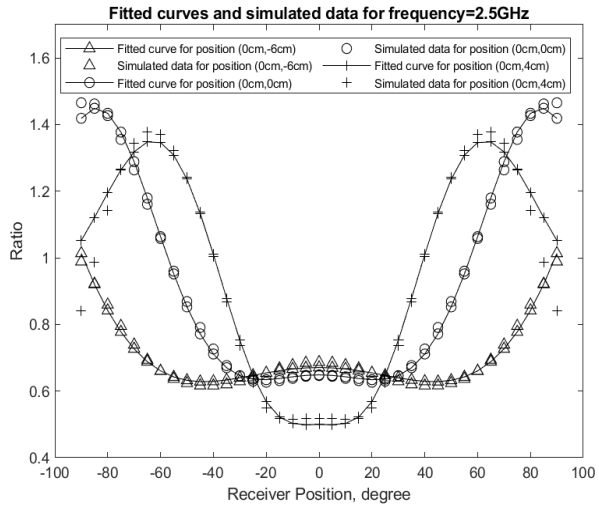


(a)

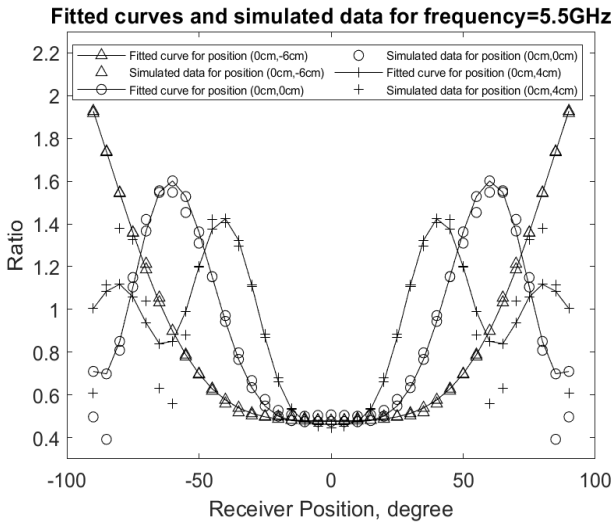


(b)

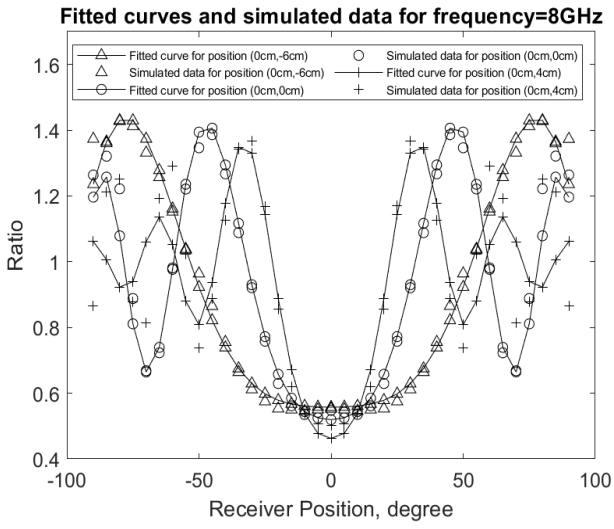


(c)

Figure 5.2: Fitted curves and simulated data for 3 different positions of Al rod and 3 different frequencies.

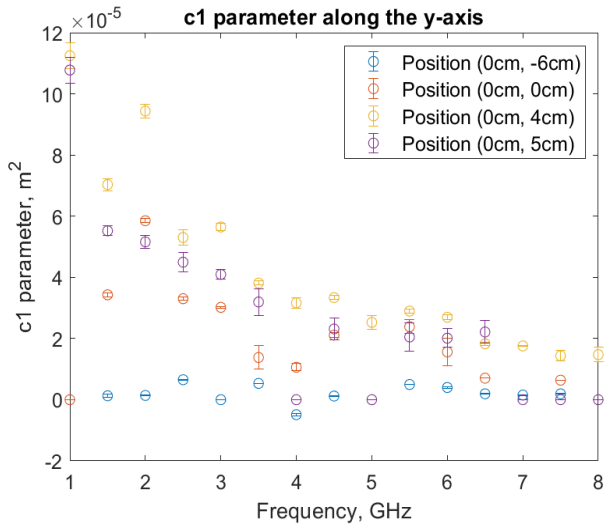


(a) Parameter $c_1$

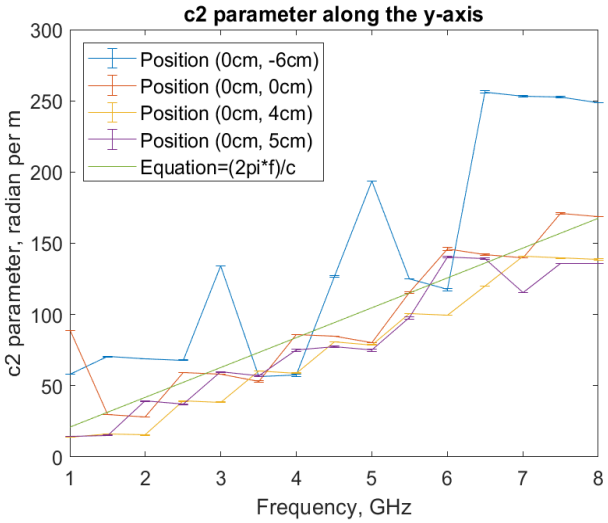


(b) Parameter $c_2$

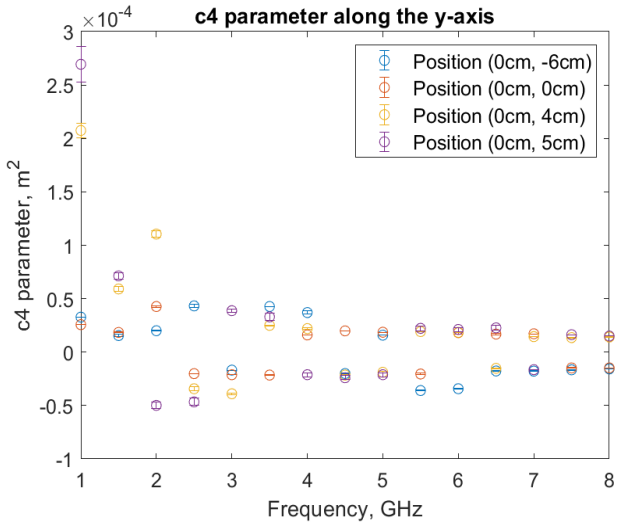


(c) Parameter $c_4$

Figure 5.3: Parameters for 4 different positions of Al rod.

Al rod's positions that the effects of the 2nd part of (5.18) were almost zero as the effects of the parameter $c_1$ were zero for fitting the ratio curves. Hence, when (5.18) was used for fitting the ratio curves, the effects of $c_1$ were neglected.

It is obtained from Fig. 5.3c that the values of $c_4$ were almost linear except for lower frequencies of the Al rod's positions - (0cm, 4cm) and (0cm, 5cm). It is also demonstrated that the values of $c_4$ and $c_2$ played vital roles in fitting the ratio curves using (5.18). The values of $c_2$ were increased if the values of the frequencies were increased for different Al rod's positions. It is known from (5.18) that $c_2$ was frequency-dependent. Hence, the values of $c_2$ for different Al rod's positions were determined using Equation = $\frac{2\pi f}{c}$, where f is the frequency. After that, $2\pi$ or 180° was replaced by the original parameter $c_3$ in the fitting equation (5.18). New values of $c_2$ which were estimated for each frequency from Equation = $\frac{2\pi f}{c}$ were placed in (5.18) and the parameter $c_4$ were replaced by the parameter $c_1$ for refitting the ratio curves for each Al rod's position.

The ratio curves were refitted with the new considered conditions and the values of $c_1$, and $c_3$ were again evaluated. The values of $c_3$ for different Al rod's positions are shown in Fig. 5.4.

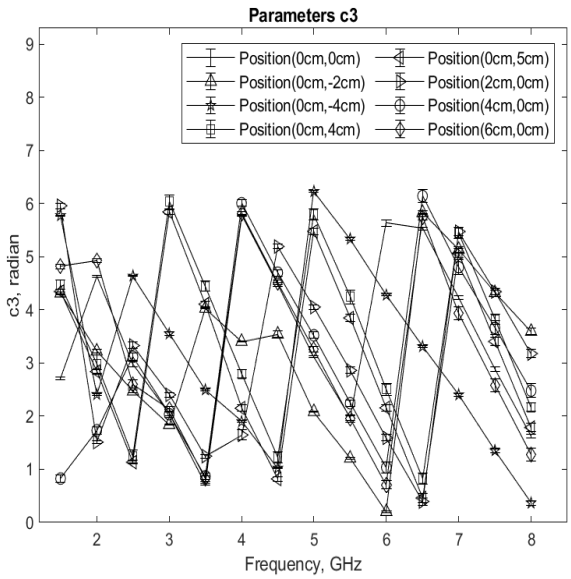


Figure 5.4: Parameter $c_3$.

It is observed from the refitted values for the parameter $c_1$ for different Al rod's positions that the values of $c_1$ were almost linear and nearby for each frequency point except the lower frequencies. The values of $c_1$ were averaged for every frequency and Al rod's position. The averaged value of $c_1$

was found as $1.93 \times 10^{-5}\ m^2$.

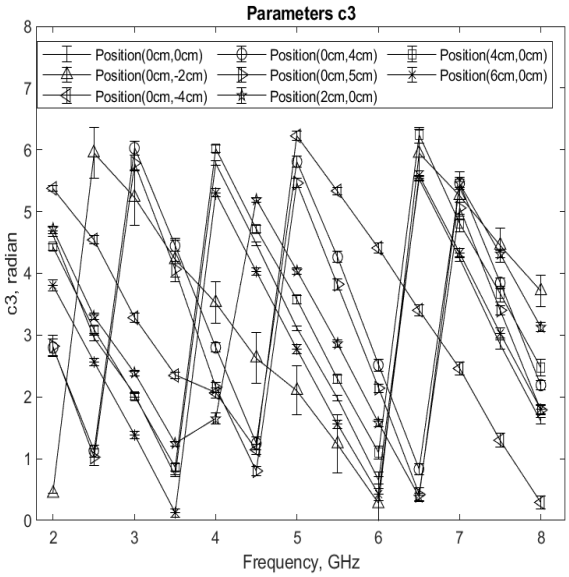


Figure 5.5: Parameter $c_3$.

Finally, the ratio curves were refitted again for all frequencies and different Al rod positions. The values of $c_3$ were determined as shown in Fig. 5.5. It is observed from Fig. 5.5 that the values of $c_3$ for different Al rod positions followed the sawtooth waveforms. The starting points and widths of each period were varied for different Al rod's positions. From these waveshapes of $c_3$ displayed in Fig. 5.5, it can be said that the propagated electric fields caused phase shift at the receiver array depending on the frequency points when Al rod was moved from one position to another position along the Y-axis (x=0) and X-axis (y=0) inside the sensing chamber of the portable device.

### 5.1.4 Conclusion

The mathematical modeling was proposed for E-field intensities at the receiver array of the simulated system and the values of parameters $c_1$, $c_2$, and $c_3$ were evaluated. The values of the parameter $c_1$ obtained from the fitting equation (5.18) were conveyed different conditions for lower frequencies than higher frequencies. It is observed from the values of $c_1$ that the parameter $c_1$ depends on the positions of Al rod in the sensing chamber. The parameter of $c_3$ depends on the operating frequencies of the portable system and also on the position of the Al rod in the sensing chamber. Hence, the equation (5.18) needs to be modified by extracting the equations for the

parameters $c_1$ and $c_3$ using two conditions - the operating frequencies of the portable system and different Al rod's positions in the sensing chamber.

## 5.2 Modified Mathematical Modeling

### 5.2.1 Introduction

This subsection represents the modified mathematical equation for providing the ratio of E-field intensities at the receiver array of the portable system. The modified equation was refitted and the values of different parameters were obtained using a robust multi-dimensional fitting procedure [83].

### 5.2.2 Methodology

The modified equation can be written as Equation (5.23). Equation (5.23) was used to extract four parameters that had their own characteristics.

$$Ratio = 1 + (\frac{F_1(v')^2}{2(u')^2(w')^2})^2 + \frac{F_1(v')^2}{(u')^2(w')^2} cos(F_2(v' - w') + 2\pi F_3) \tag{5.23}$$

where,

$F_1 = C - D((x')^2 + (y')^2)\ (m^2)$

$u' = \sqrt{(l + y')^2 + (x')^2}\ (m)$,

$w' = \sqrt{(qcos\theta - y')^2 + (qsin\theta - x')^2}\ (m)$,

$v' = \sqrt{(l + qcos\theta)^2 + (qsin\theta)^2}\ (m)$

$F_3 = (1 - \frac{F_4}{c}) + \lfloor \frac{F_4}{c} \rfloor\ (unitless)$

$F_3 = B - fu'$

$or, F_4 = 10^9 \times (B - fu')\ ms^( - 1)$

$F_2 = \frac{2 \times 10^9 \pi f}{c}\ (ms^{-1})$

The parameter A was unitless and scaled the Al rod position to represent the near-field condition instead of the far-field consideration used in Equation (5.18) and $F_2$ represented $c_2$ of Equation (5.18). $F_3$ was equivalent to $c_3$ and provided the phase shift (constrained to 0 to $2\pi$) at the receiver array due to the different positions of Al rod. $\frac{2\pi B}{c}$ was the phase shift at the reference centre (x=0,

and y-0) and should be equivalent to $\frac{\pi}{2}$ according to the theory. $F_1$ is equal to $c_1$ of Equation (5.18). Although $c_1$ was ideally represented as a constant, $c_1$ was allowed to vary as a function of Al rod's positions using an empirical relationship that was controlled by C $m^2$ and D (unitless). C was proportional to the effective radar cross-section of the Al rod at the centre (0,0) point on the X-axis where C was at its maximum value. D was a unitless empirical factor and controlled the change in effective radar cross-section of the Al rod as a function of Al rod's position due to relative beam pattern changing as a function of distance from the transmitter.

In Equation (5.23), $x'$ and $y'$ were the X-axis and Y-axis values of the Al rod's position in meters scaled by A, f was the frequency in GHz, $\theta$ was the sensor angles in radians, l=0.11 m, and q=0.09 m described the system geometry while $c = 3{\times}10^8\ ms^{-1}$ was the speed of light. Here, $u'$,$v'$, and $w'$ represented u, v, and w of Equation (5.23) scaled by A. This mathematical equation displayed the E-field intensity as a function of four variables. These are - (i) frequency from 2GHz to 8GHz, (ii) X-axis values of Al rod' positions over a range of $\pm 6\ cm$, (iii) Y-axis values of Al rod's positions over a range of $\pm 6\ cm$, and (iv) receiver positions over $\pm 90\ degrees$.

A robust multi-dimensional fitting was conducted for all the dataset. After fitting, mean, standard deviation, and normal distribution were observed for the residuals. Minimum frequencies and receiver positions for the portable system were measured using the characteristics of residuals from the fitting.

Analysis was conducted using dividing the data into training and validation sets. 3 different training and validation set were made for 21 Al rod positions and 15 frequencies shown in Fig. 5.6. For every division, dataset was divided into approximately 70 $\%$ training and 30 $\%$ validation to validate the modified mathematical equation (5.23). From Fig. 5.6, it is observed that data of all frequencies for 6 positions of Al rod - (0cm, -4cm), (0cm, 4cm), (0cm, 5cm), (4cm, 4cm), (6cm, 3cm), and (6cm, 0cm) and data of 21 Al rod position for 8GHz were used as validation set for Try-1. All other data were used as training dataset and training data was fitted using Equation (5.23) and A, B, C and D were evaluated.

For Try-2 shown in Fig. 5.6, validation dataset was made using data of all frequencies for 3 Al rod's positions - (4cm, 4cm), (6cm, -2cm), and (6cm, 3cm) and 21 positions for 7GHz, 7.5GHz, and 8GHz frequencies and all other data were considered as training dataset. Training dataset was fitting using Equation (5.23) for Try-2 and A, B, C, and D parameters were evaluated.

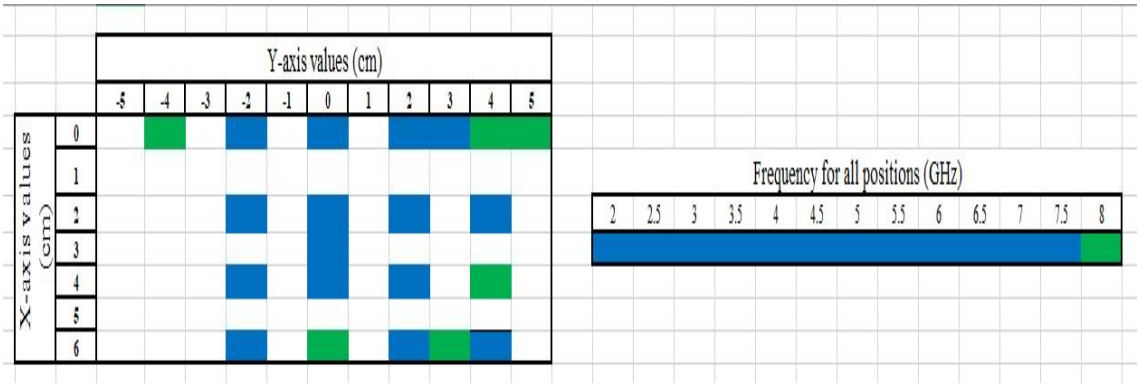


(a) First dataset named as Try-1

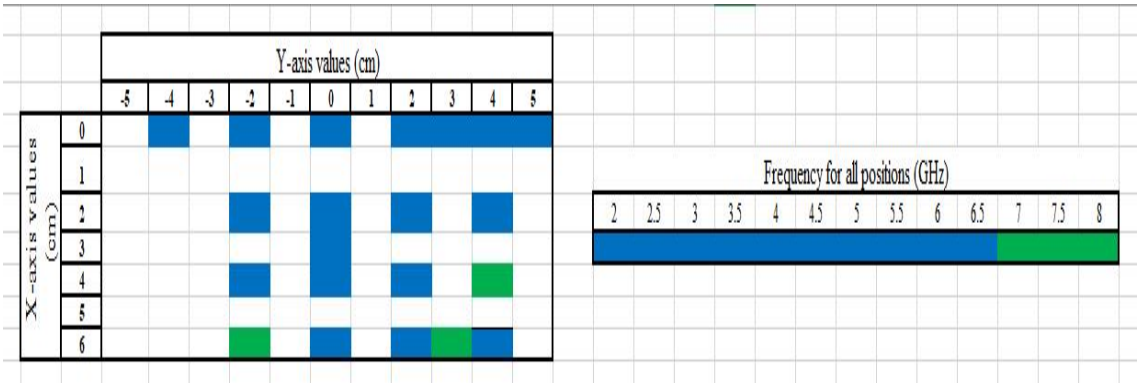


(b) Second dataset named as Try-2

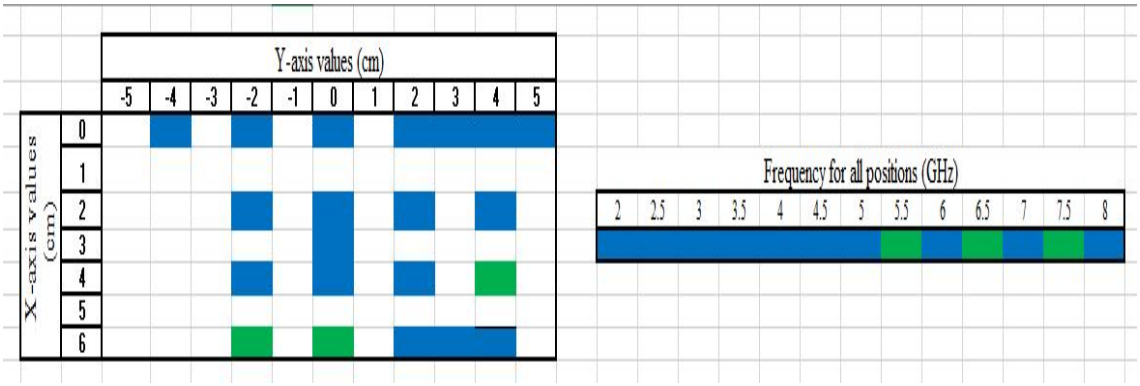


(c) Third dataset named as Try-3

Figure 5.6: 3 different training and validation dataset for analysis.

For Try-3 shown in Fig. 5.6, validation dataset was considered using data of all frequencies for 3 Al rod's positions - (4cm, 4cm), (6cm, -2cm), and (6cm, 0cm) and 21 positions for 5.5GHz, 6.5GHz, and 7.5GHz frequencies and all other data were assumed as training dataset. Training dataset was fitting further using Equation (5.23) for Try-3, and the values of A, B, C, and D parameters were calculated.

### 5.2.3 Result and Discussion

The modified equation was fitted in TableCurve 3D [83] and the fitting constants were obtained using a robust multi-dimensional fitting procedure. The fitting returned an $r^2 = 0.92$ for Al rod positions situated within 6cm radius of the sensing chamber and the operating frequencies from 2GHz to 8GHz. According to the discussion based on the parameters of initial mathematical equations in **section 5.1** and after observing the fitting using the modified equation, the frequencies less than 2GHz were excluded for the final fitting.

Equation (5.23) agreed with simulated results to within -0.00343 (-1.3%) $\pm$ 0.092 ($\pm$ 10%). The p-values for all parameters were less than 0.01, and F-value was 30183.28. Outliers were removed using Chauvenet's criterion so that the residuals were remained within $\pm$ 3 sd (standard deviation). The values of mean, standard error, and data points were evaluated as -0.004161753, 0.092481711, and 8357 respectively. The residuals following Equation (5.23) were normally distributed. The residuals obtained from the fitting and the normal distribution of residuals are shown in Fig. 5.7, and Fig. 5.8. Fitting Equation (5.23) to the data given following values:

A = 0.871 $\pm$ 0.002 (unitless),

B = 0.748 $\pm$ 0.0002 (m$s^{-1}$),

C = 0.0015 $\pm$ 7 $\times$ $10^{-06}$ m$s^2$, and

D = 0.229 $\pm$ 0.004 (unitless)

The values of A, B, C, and D had small uncertainties, with A being consistent with the ideal value of l and B being close to the theoretical value of 0.75. While $F_1$ was ideally a constant = C, a term (controlled by D) was necessary to improve the agreement with the simulated data by reducing the ratio (primarily through the third term of Equation (5.23)) as the rod moves away from x = 0 and y = 0.

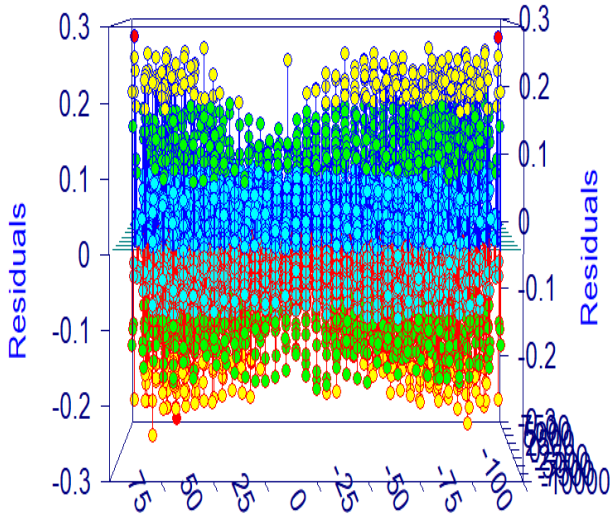


Figure 5.7: The values of residuals.

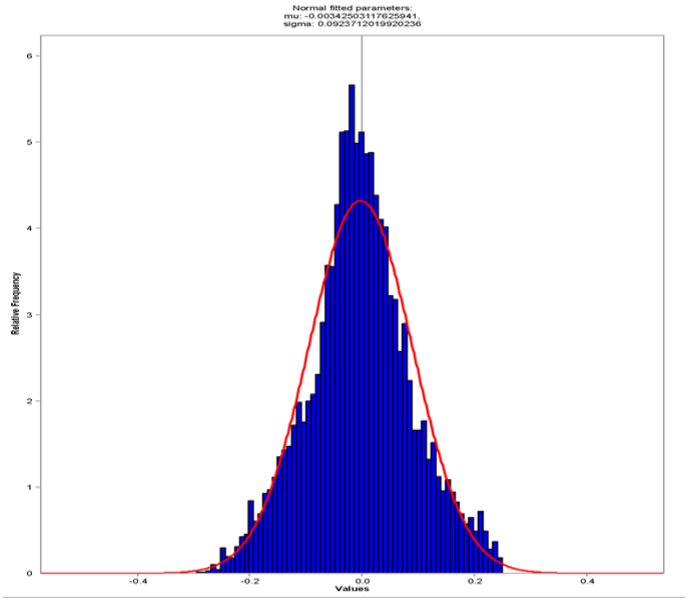


Figure 5.8: Normal distribution of the residuals.

Fig. 5.9, and Fig. 5.10 represents the simulated data obtained from CST Microwave solver and fitted estimated from Equation (5.23) using the fitting parameters as a function of Al rod positions, frequencies, and receiver positions. Fig. 5.9 represents the E-field intensity as a function of frequencies and receiver positions for 3 different positions of Al rod - (0cm, 0cm), (0cm, 2cm), and (4cm, 0cm) respectively. Fig. 5.10 illustrates the ratio of the E-field intensity for 2GHz and 4GHz frequencies as a function of receiver positions and Al rod positions on the Y-axis (x=0) and the X-axis (y=0).

After considering the operating frequency 2 GHz to 5 GHz and the receiver array in angles from -80° to 80°, $r^2 = 0.93$ was obtained from the fitting of Equation (5.23). The p-values for all parameters were less than 0.01. From the lower frequency analysis, the residuals were fell within the standard deviation of $\pm$ 3 shown in Fig. 5.11 except for the ratio of E-field intensities of Al rod's position (6cm, 2cm) at 5 GHz. Chauvenet's criterion was not needed to be run for removing this one outlier.

The values of A, B, C, and D constant were achieved as 0.874 $\pm$ 0.003, 0.748 $\pm$ 0.0002, 0.0015 $\pm$ $9 \times 10^{-06}$, 0.22 $\pm$ 0.004 respectively from that fitting. It can be said that the portable breast cancer detection system with the lower operating system from 2 GHz to 8 GHz can be considered for detecting breast lesions.

E-field intensities for each Al rod's position at every frequency point from 2 GHz to 8 GHz were estimated by the multiplication of the fitted ratio curve of the same Al rod's position at each frequency acquired from Equation (5.23) and open-space E-field intensities at that frequency. The evaluated E-field intensities for each Al rod's position at every frequency from 2 GHz to 8 GHz were averaged and the ratio of averaged E-field intensities of each Al rod's position was estimated by the division of the E-field intensities for each Al rod position by the averaged open-space E-field intensities. The ratio of the averaged E-field intensities for Al rod's positions along the X-axis and Y-axis were represented in Fig. 5.12. The characteristics of the ratio curves obtained from Fig. 5.12 were included in Table 5.1 to Table 5.4.

From Fig. 5.12 and Table 5.1 to Table 5.4, it is said that the ratio curves of averaged E-field intensities acquired from the modified fitting equation (5.23) were provided as the same characteristics as the ratio curves obtained from the simulation and validated the previously considered two condition written in **chapter 5**. The fitted ratio curve peak points were shifted as the same as

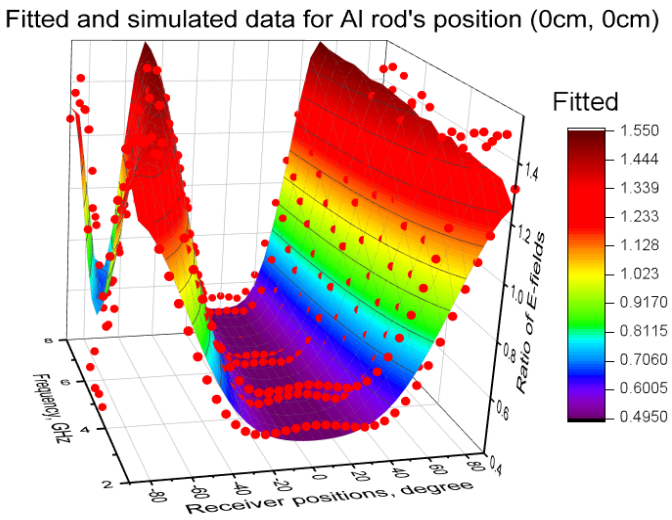


(a) Fitted and simulated data for Al rod's position (0cm, 0cm)

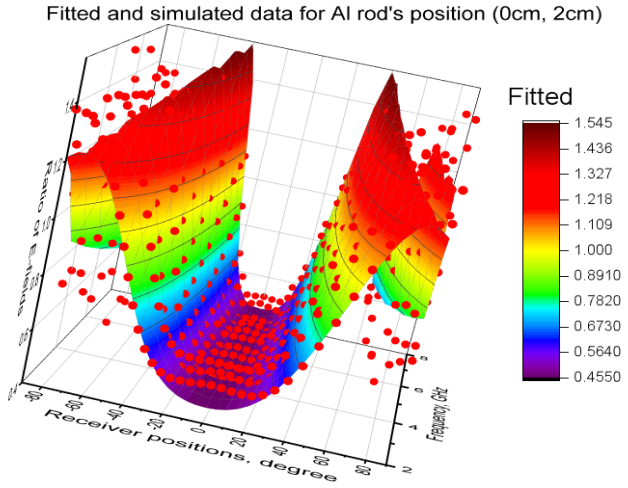


(b) Fitted and simulated data for Al rod's position (0cm, 2cm)

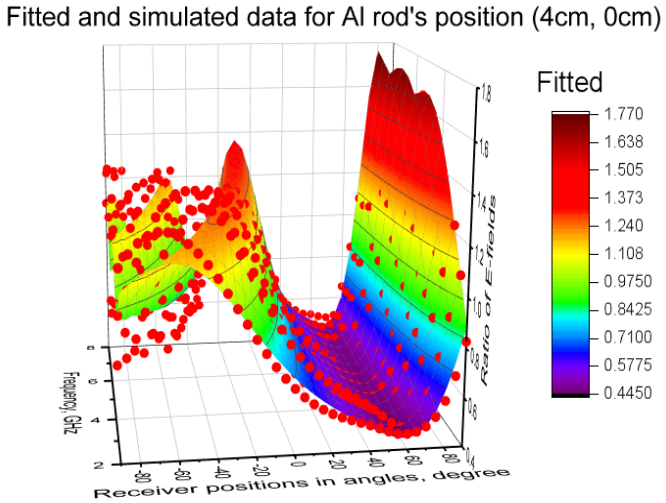


(c) Fitted and simulated data for Al rod's position (4cm, 0cm)

Figure 5.9: Fitted (surface) and simulated data (points) for Al rod's position (0cm, 0cm), position (0cm, 2cm) and position (4cm, 0cm).

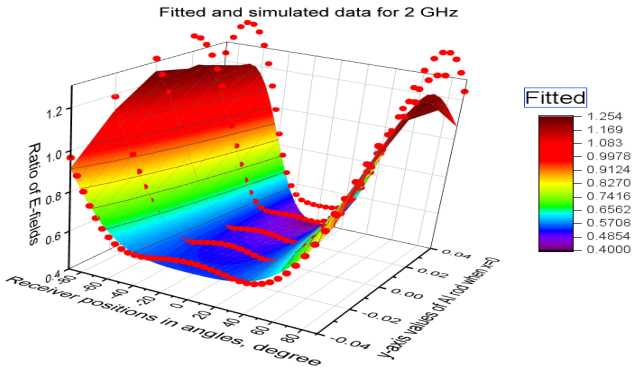


(a) Different positions of Al rod along the Y-axis (x=0) for frequency = 2 GHz

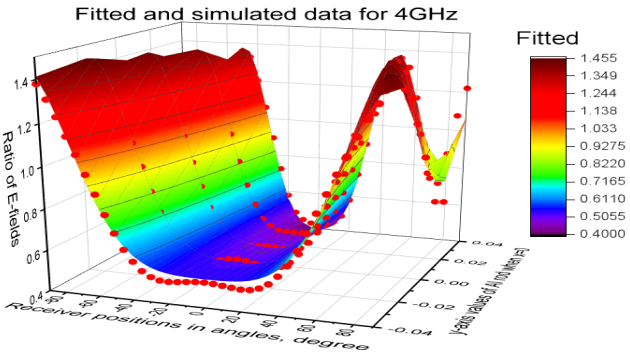


(b) Different position of Al rod along the Y-axis (x=0) for frequency = 4 GHz

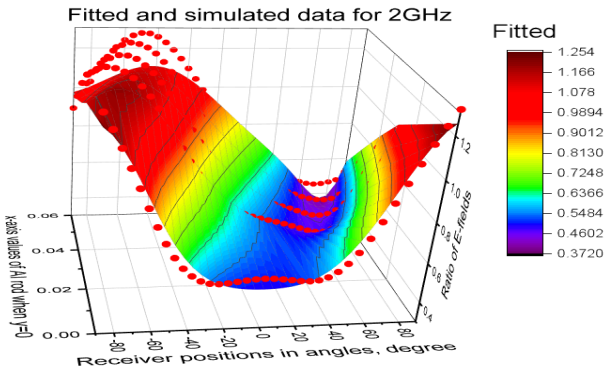


(c) Different position of Al rod along the X-axis (y=0) for frequency = 2 GHz

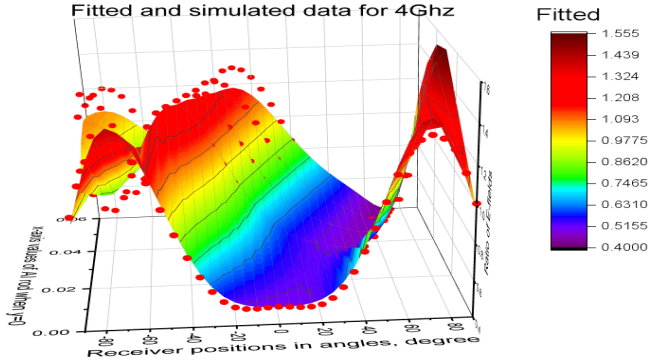


(d) Different position of Al rod along the X-axis (y=0) for frequency = 4 GHz

Figure 5.10: Fitted (surface) and simulated data (points) for 2 GHz and 4 GHz.

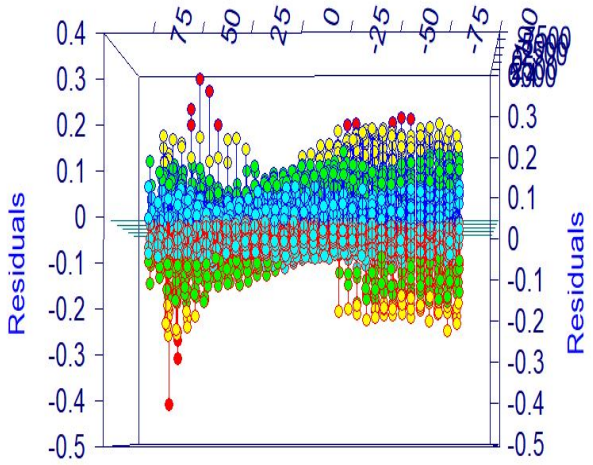


Figure 5.11: The values of residuals for the frequency range from 2 GHz to 5 GHz.

Table 5.1: Al rod's behaviors along the X-axis for the fitted conditions obtained from mathematical modeling shown in Fig. 5.12

| Positions of Al rod | Maximum peak's conditions at left side | | Maximum peak's conditions at right side | |
|---|---|---|---|---|
| | Receiver Positions | Ratio of E-fields | Receiver Positions | Ratio of E-fields |
| (-4cm, 0cm) | -85° ± 5° | 1.41 | 15° ± 5° | 1.21 |
| (-2cm, 0cm) | -75° ± 5° | 1.35 | 40° ± 5° | 1.26 |
| (0cm, 0cm) | -55° ± 5° | 1.30 | 55° ± 5° | 1.30 |
| (2cm, 0cm) | -40° ± 5° | 1.26 | 75° ± 5° | 1.35 |
| (3cm, 0cm) | -25° ± 5° | 1.23 | 80° ± 5° | 1.38 |
| (4cm, 0cm) | -15° ± 5° | 1.21 | 85° ± 5° | 1.41 |
| (5cm, 0cm) | -5° ± 5° | 1.17 | more than 90° | unknown |

the simulated ratio curves peak points if the Al rod's position shifted from the negative X-axis to the positive X-axis shown in Table 5.1 to Table 5.3. The same condition was observed for the change of the Al rod's position along the Y-axis shown in Fig. 5.12 and Table 5.4. It is also observed from Fig. 5.12 that the widths of the ratio curves were changed the same as the simulated ratio curves' widths if the Al rod's position was moved from the negative Y-axis to the positive Y-axis.

### 5.2.4 Analysis of 3 different training and validation dataset

From Fig. 5.6, R-squared values for Try-1, Try-2 and Try-3 were 0.91, 0.93, and 0.91 respectively. All p-values were less than 0.01 for 3 different cases. Fitting Equation (5.23) to training data -

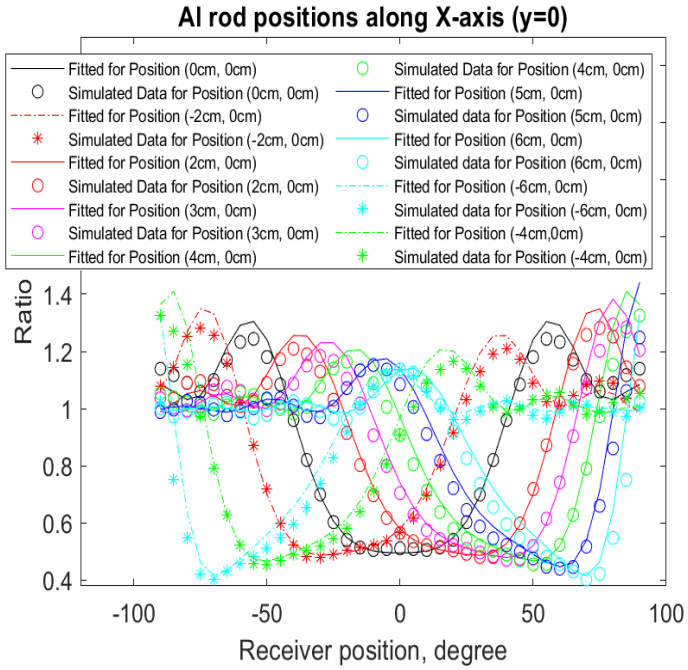


(a) Ratio of E-fields for Al rod's positions along the X-axis.

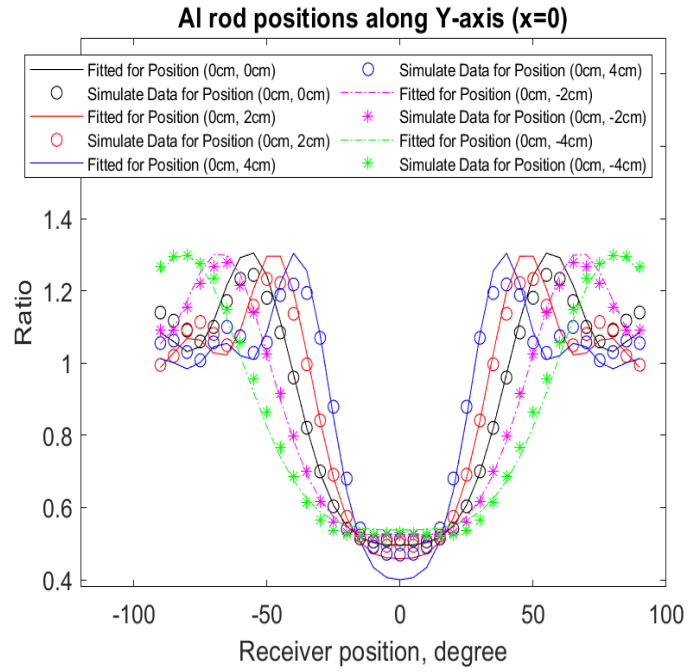


(b) Ratio of E-fields for Al rod's positions along the Y-axis.

Figure 5.12: Ratio of E-fields for different positions of Al rod along the X-axis and Y-axis.

Table 5.2: Difference between fitted and simulated Al rod's behaviors along the X-axis shown in Fig. 5.12

| Positions of Al rod | Receiver positions at maximum peak (Left side) | | Receiver positions at maximum peak (Right side) | |
|---|---|---|---|---|
| | Fitted | Simulated | Fitted | Simulated |
| (-4cm, 0cm) | -85° ± 5° | -90° ± 5° | 15° ± 5° | 20° ± 5° |
| (-2cm, 0cm) | -75° ± 5° | -75° ± 5° | 40° ± 5° | 40° ± 5° |
| (0cm, 0cm) | -55° ± 5° | -55° ± 5° | 55° ± 5° | 55° ± 5° |
| (2cm, 0cm) | -40° ± 5° | -40° ± 5° | 75° ± 5° | 75° ± 5° |
| (3cm, 0cm) | -25° ± 5° | -30° ± 5° | 80° ± 5° | 85° ± 5° |
| (4cm, 0cm) | -15° ± 5° | -10° ± 5° | 85° ± 5° | 90° ± 5° |
| (5cm, 0cm) | -5° ± 5° | -10° ± 5° | more than 90° | more than 90° |

Table 5.3: Difference between Al rod's behaviors along the X-axis from Fig. 5.12

| Positions of Al rod | Minimum peak's conditions (fitted) | | Minimum peak's conditions (simulated) | |
|---|---|---|---|---|
| | Receiver Positions | Ratio of E-fields | Receiver Positions | Ratio of E-fields |
| (-4cm, 0cm) | -50° ± 5° | 0.47 | -50° ± 5° | 0.46 ± 0.22 |
| (-2cm, 0cm) | -30° ± 5° | 0.49 | -30° ± 5° | 0.48 ± 0.22 |
| (0cm, 0cm) | 0° ± 5° | 0.50 | 0° ± 5° | 0.53 ± 0.22 |
| (2cm, 0cm) | 30° ± 5° | 0.49 | 30° ± 5° | 0.48 ± 0.22 |
| (3cm, 0cm) | 40° ± 5° | 0.48 | 40° ± 5° | 0.47 ± 0.22 |
| (4cm, 0cm) | 50° ± 5° | 0.47 | 55° ± 5° | 0.46 ± 0.22 |
| (5cm, 0cm) | 60° ± 5° | 0.45 | 60° ± 5° | 0.44 ± 0.22 |

Table 5.4: Al rod's behaviors along the Y-axis for the fitted conditions obtained from mathematical modeling shown in Fig. 5.12

| Positions of Al rod | Ratio of E-fields | Widths obtained from | | Receiver positions at maximum peaks | |
|---|---|---|---|---|---|
| | | Fitted | Simulation | Left side | Right side |
| (0cm, -4cm) | 1.30 | 160 | 160 ± 5 | -80° ± 5° | 80° ± 5° |
| (0cm, -2cm) | 1.30 | 140 | 130 ± 5 | -70° ± 5° | 70° ± 5° |
| (0cm, 0cm) | 1.30 | 110 | 110 ± 5 | -55° ± 5° | 55° ± 5° |
| (0cm, 2cm) | 1.30 | 100 | 100 ± 5 | -50° ± 5° | 50° ± 5° |
| (0cm, 4cm) | 1.30 | 80 | 80 ± 5 | -40° ± 5° | 40° ± 5° |

Try-1, Try-2, and Try-3 provided the values of A, B, C, and D written in Table 5.5.

Mean, and standard deviation of the residuals for 3 training datasets and testing datasets were calculated provided in Table 5.6. Residuals for training and testing datasets followed normal distribution shown in Fig. 5.13 and Fig. 5.13.

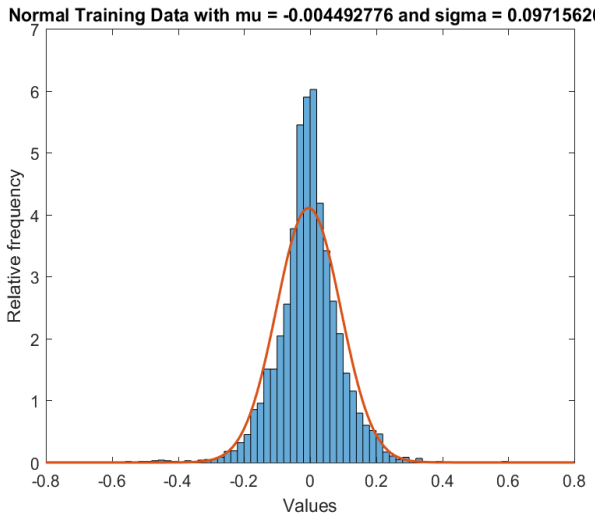


(a) Training dataset for Try-1

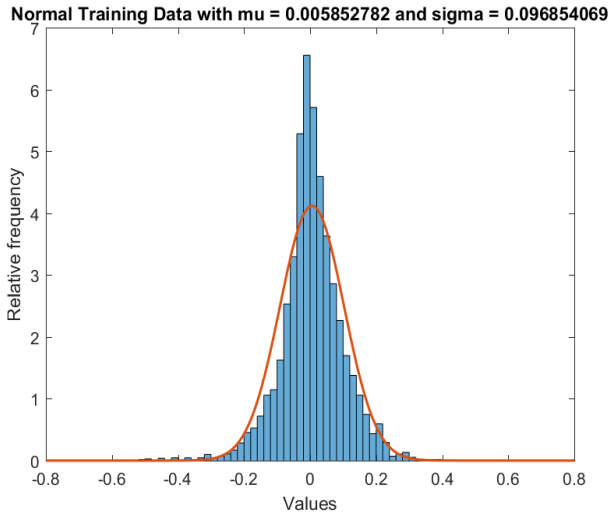


(b) Training dataset for Try-2

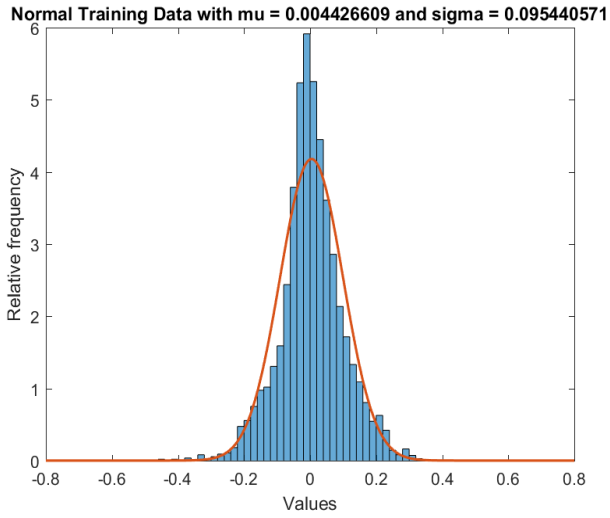


(c) Training dataset for Try-3

Figure 5.13: Normal distribution of the residuals for 3 training datasets shown in Fig. 5.6.

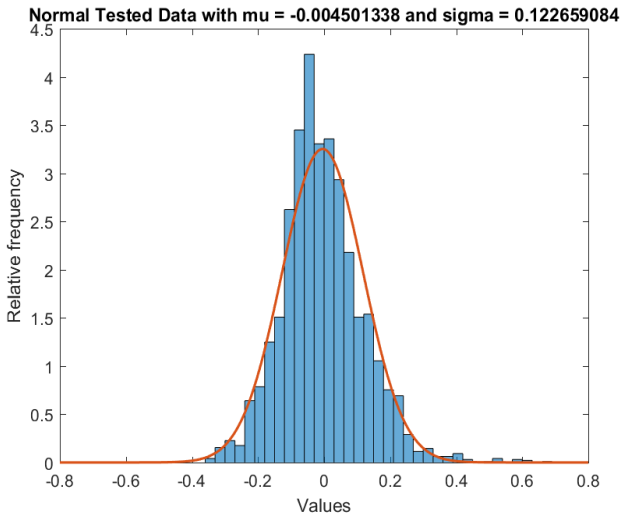


(a) Tested dataset for Try-1

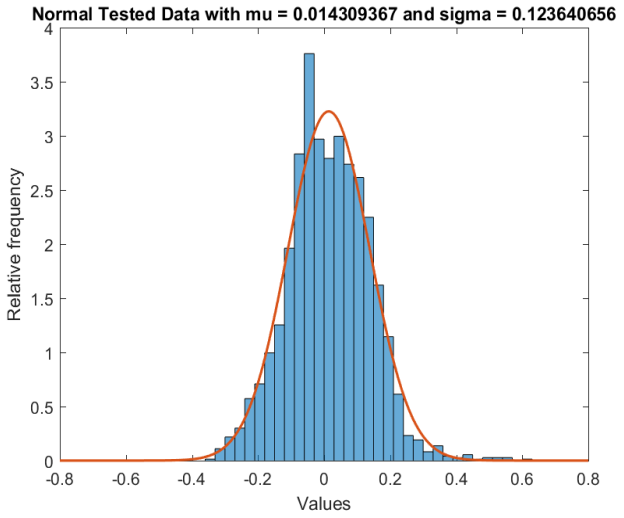


(b) Tested dataset for Try-2

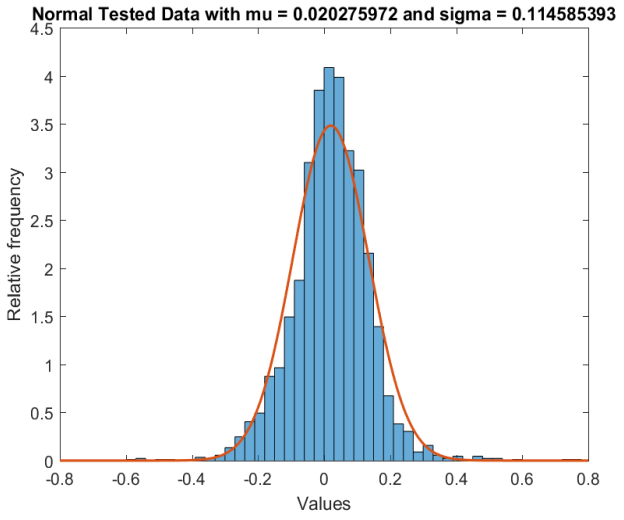


(c) Tested dataset for Try-3

Figure 5.14: Normal distribution of the residuals for 3 testing datasets shown in Fig. 5.6.

Table 5.5: Values of Parameters evaluated from fitting for 3 different training and validation datasets shown in Fig. 5.6

| Datasets | A (unitless) | B ($ms^{-1}$) | C ($ms^2$) | D (unitless) |
|---|---|---|---|---|
| Try-1 | 0.864 $\pm$ 0.002 | 0.748 $\pm$ 0.0002 | 0.0015 $\pm$ 7 $\times$ $10^{-06}$ | 0.214 $\pm$ 0.005 |
| Try-2 | 0.87 $\pm$ 0.002 | 0.749 $\pm$ 0.0002 | 0.0015 $\pm$ 7 $\times$ $10^{-06}$ | 0.23 $\pm$ 0.005 |
| Try-3 | 0.87 $\pm$ 0.002 | 0.749 $\pm$ 0.0002 | 0.0015 $\pm$ 7 $\times$ $10^{-06}$ | 0.24 $\pm$ 0.004 |

Table 5.6: Mean and Standard Deviation from fitting for 3 different training and validation datasets shown in Fig. 5.6

| Datasets | Try-1 | | Try-2 | | Try-3 | |
|---|---|---|---|---|---|---|
| | Mean | Standard Deviation | Mean | Standard Deviation | Mean | Standard Deviation |
| Training | -0.0045 | 0.097 | 0.0059 | 0.097 | 0.0044 | 0.095 |
| Testing | -0.0045 | 0.12 | 0.014 | 0.12 | 0.020 | 0.11 |

Fitted validation data for the considered validation points were calculated using the fitting parameters values and compared with simulated data obtained from CST Microwave software shown in Fig. 5.15 for Try-1.

For Try-2, fitted validated data were evaluated for the assumed validated points using the fitted parameters and compared with the simulated values shown in Fig. 5.16.

For Try-3, validation data were also calculated for the considered validated points using the obtained fitted parameters and compared with the simulated values shown in Fig. 5.17.

### 5.2.5 Conclusion

This section evaluates a 3D mathematical modeling for fitting the ratio of E-fields for different positions of Al rod with an R-squared value of 0.92. The residuals after fitting using the mathematical modeling stayed within the standard error of $\pm$ 3. The values of the parameters A, B, C, and D were obtained from TableCurve 3D software after the fitting.

## 5.3 Conclusion

This chapter provides the derivation of the mathematical equation for fitting the ratio of E-field intensities. The characteristics of the parameters obtained from the fitting were evaluated. The fitted and simulated ratio of E-field intensities were compared. The averaged ratio of fitted E-field

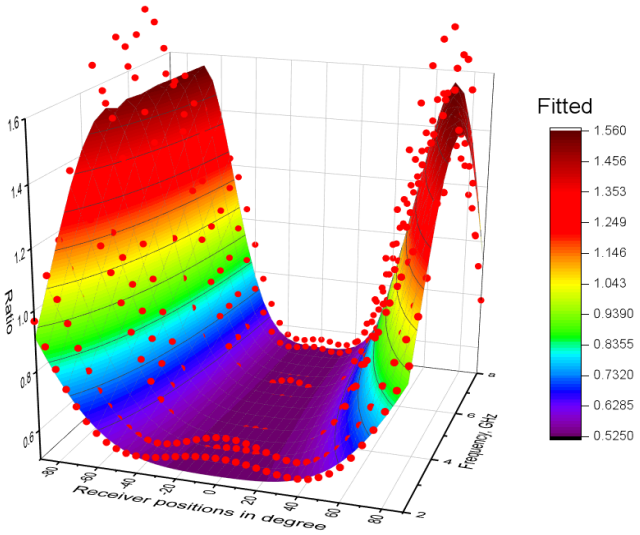


(a) Fitted and simulated data for Al rod's position (0cm, -4cm)

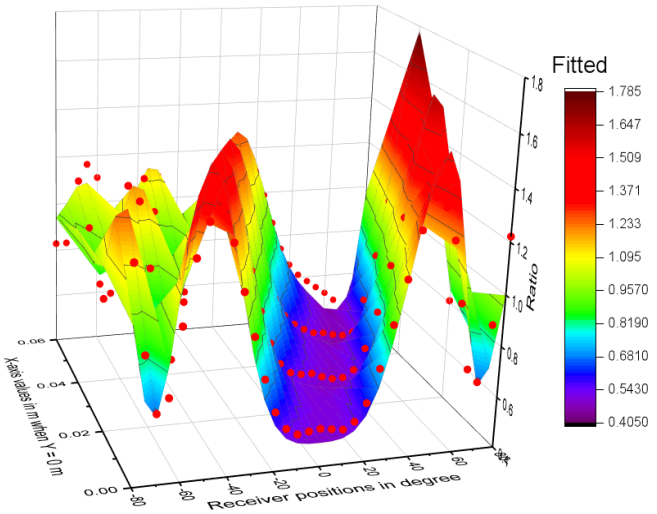


(b) Fitted and simulated data for X-axis values when y = 0m and Frequency = 8GHz

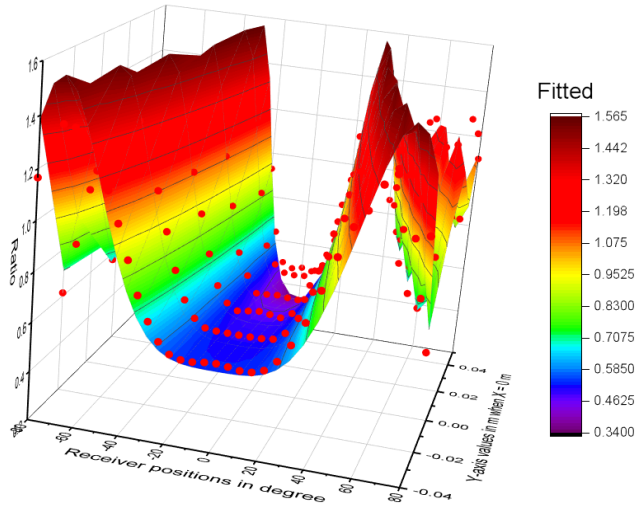


(c) Fitted and simulated data for Y-axis values when x = 0m and Frequency = 8GHz

Figure 5.15: Fitted (surface) and simulated data (points) for Al rod's position (0cm, -4cm), Y=0 and X=0 values when Frequency = 8GHz for Try-1.

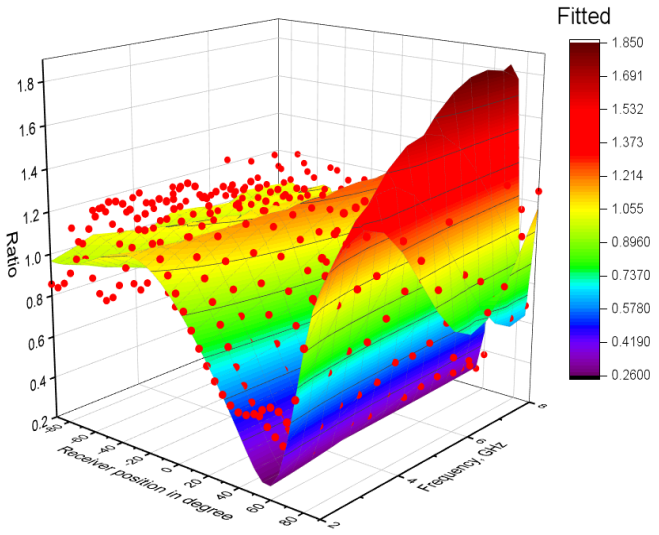


(a) Fitted and simulated data for Al rod's position (6cm, 3cm)

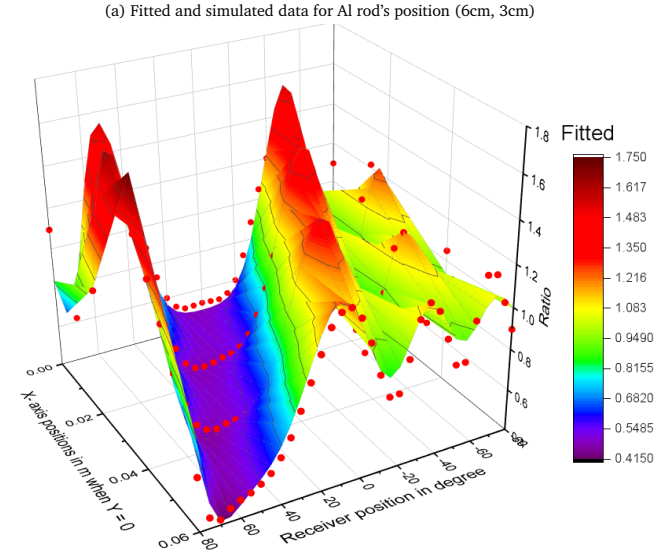


(b) Fitted and simulated data for X-axis values when y = 0m and Frequency = 7.5GHz

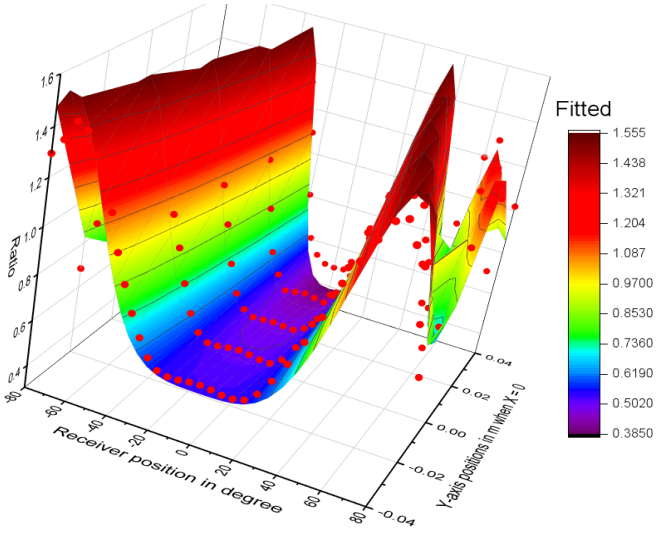


(c) Fitted and simulated data for Y-axis values when x = 0m and Frequency = 7.5GHz

Figure 5.16: Fitted (surface) and simulated data (points) for Al rod's position (6cm, 3cm), Y=0 and X=0 values when Frequency = 7.5GHz for Try-2.

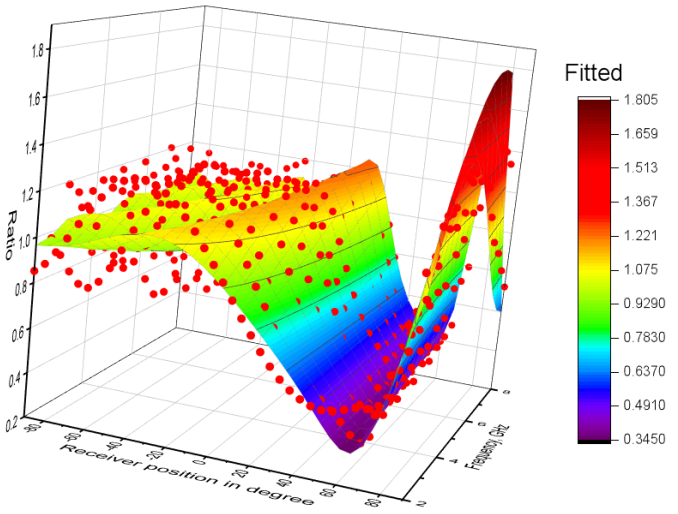


(a) Fitted and simulated data for Al rod's position (6cm, 3cm)

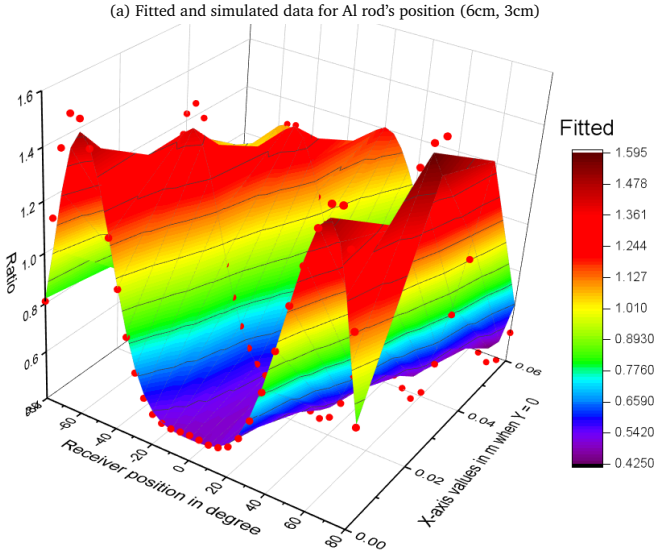


(b) Fitted and simulated data for X-axis values when y = 0m and Frequency = 5.5GHz

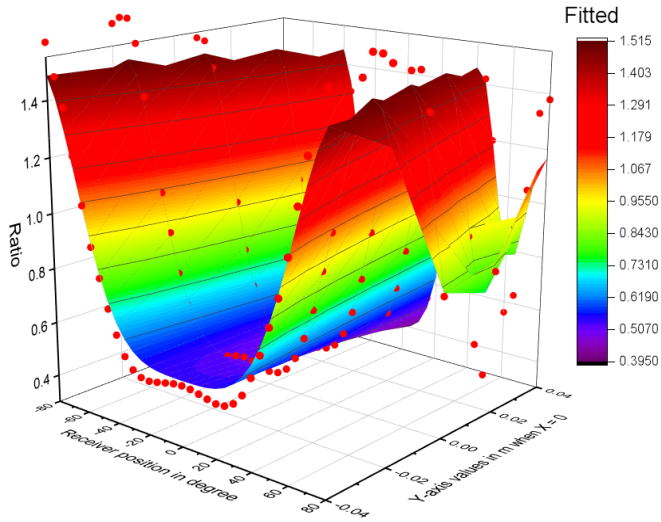


(c) Fitted and simulated data for Y-axis values when x = 0m and Frequency = 5.5GHz

Figure 5.17: Fitted (surface) and simulated data (points) for Al rod's position (6cm, 2cm), Y=0 and X=0 values when Frequency = 5.5GHz for Try-3.

intensities also represented the same characteristics as the averaged ratio of simulated E-fields when Al rod's position was moved along the Y-axis (x = 0) and X-axis (y = 0). The optimal frequency range from 2 GHz to 5GHz was estimated using mathematical modeling for the simulated system.

# Chapter 6

# Conclusions of the Thesis and Future Work

## 6.1 Conclusions

Microwave techniques enter the breast sensing field with the potential to overcome the disadvantages of conventional breast sensing devices like MRI, X-ray, and Ultrasound for early-stage breast cancer detection. The research on the breast microwave sensing system has been going on to achieve higher sensitivity as well as make the modality more cost-effective and available. However, the challenge remains to build a Microwave breast cancer detection system that will be portable and easily installable for the Low and Middle-Income Countries (LMIC) and even in remote regions of developed countries like Canada. Other advantages of the Microwave modality that needs to be delivered will be flexibility, simplicity, accessibility, and comfortability for women. Otherwise, as the system should have the potential to operate without the help of an experienced person, women can manage the device by themselves. This thesis project was conducted on the portable microwave breast cancer detection system for LMIC and remote regions.

Before researching the optimal hardware setup of the portable system, this thesis was focused on the simulated microwave breast cancer detection system with the transmitter and receiver antennas to make the device portable and easily accessible. The portable system was simulated in a 3D environment for getting the bottom of the design of the portable system. A horn antenna was designed in Antenna Magus software with the same characteristics of the horn antenna used in the laboratory and the performance of the antenna was estimated. When the desirable performance was observed, the horn antenna was imported in the CST Microwave solver and the characteristics of the horn antenna such as transmission and reflection coefficients were compared with the horn antenna used experimentally for different conditions. A bandwidth agreement of 90% at -10dB

between the simulated reflection coefficient obtained from CST Microwave solver and the measured reflection coefficient of the experimental horn antenna estimated from the Vector Network Analyzer (VNA). After getting the desirable agreement for transmitter antenna, the whole portable system was designed and simulated from 1 GHz to 8 GHz in CST Microwave Solver with 37 receiver points for avoiding the complexity of the system.

For the analysis of the propagated electric fields inside the sensing chamber of the portable system, an Al rod was used as a point-like scatterer. Al rod was placed at different places inside the sensing chamber within 6cm radius and electric fields (E-fields) were evaluated at the receiver array. The maximum peak occurring points of the ratios of the averaged E-fields were shifted when the Al rod was moved from the negative X-axis (y = 0) to the positive X-axis (y = 0). The same behaviors of the maximum peak occurring points of the ratio curves were also found because of shifting the Al rod along with the Y-axis (x = 0). The widths of the ratio curves were decreased when the Al rod was moved from the negative Y-axis (x = 0) to the positive Y-axis (x = 0) because the peaks of the ratios shifted to larger angles as the Al rod moved from the positive Y-axis (closet to the receiver) to the negative Y-axis (closet to the transmitter). The same characteristics were observed when Al rod was moved from the negative X-axis to the positive X-axis for different values of Y-axis such as y = -2cm or y = 2cm.

A 3D mathematical equation was developed for explaining the behaviors of the received E-fields due to different positions of the Al rod and producing a large number of the received E-fields due to the Al rod positioned at different points inside the sensing chamber. The fitting provides $r^2 = 0.92$ after removing the outliers using Chauvenet's criterion for the operating frequencies from 2GHz to 8Ghz. Equation (5.23) agreed with simulated results to within -0.00343 (-1.3%) $\pm$ 0.092 ($\pm$ 10%), the p-values for all parameters were less than 0.01. The values of A, B, C, and D constants of the mathematical modeling were acquired as 0.871 $\pm$ 0.002, 0.748 $\pm$ 0.0002, 0.0015 $\pm$ $7 \times 10^{-06}$, and 0.229 $\pm$ 0.004. The ratios of the averaged fitted E-field intensities were evaluated for different positions of the Al rod. The ratio curves obtained from fitting the mathematical equation provided the same behaviors as the ratio curves estimated using the simulation data. The peak maximum occurring points of the ratio fitted curves were shifted when the Al rod was moved from the negative X-axis (y = 0) to the positive X-axis (y = 0). The same types of behaviors were observed for the fitted ratio curves when the Al rod was changed its positions from the negative Y-axis (x = 0) to the

positive Y-axis (x = 0). The widths of the ratio curves were decreased when the Al rod was moved from the negative Y-axis to the positive Y-axis. The optimal frequency points and the numbers of receiver points at the receiver array were analyzed for the simulated portable system using the derived mathematical equation. $r^2 = 0.93$ were found after fitting the mathematical equation for the frequency range from 2 GHz to 5 GHz and 33 receiver points at the receiver array from -80° to 80°. The residuals were found within the standard deviation of $\pm$ 3 for the lower frequency analysis and the p-values for all parameters were less than 0.01 for the fitting.

## 6.2 Future Work

A large number of data can be produced using the proposed mathematical equation within a short period instead of waiting on the simulation which is going on for 2-3 hours. The large datasets are needed for the input of the future machine learning model which will be designed to detect the positions of the Al rod inside the sensing chamber of the portable system.

The human breast has a complex structure consisting of skin, fatty tissue, fibroglandular tissue, and tumor (breast lesion). The received signal at the receiver side contains the scattering from those tissues, especially from the fibroglandular tissues. The differentiation between the scatterings from the breast lesion and the fibroglandular tissues is a difficult task. In the future, the portable system with 2 point-like scatterers can be simulated for analyzing the behaviors of the received E-fields and detecting the positions of the scatterers inside the sensing chamber using the machine learning model.

The transmitter antenna can be changed with another antenna especially for the frequency analysis less than 2 GHz. In the future, the portable system can be simulated with the new desired antenna and the behaviors of the E-fields should be analyzed for the lower frequency.

Inside of using one transmitter antenna and several receivers, several antennas can be designed which can continuously transmit and receive electromagnetic fields after considering the cost-effective and portability characteristics of the breast cancer detection system. More antennas can help to detect the positions and sizes of the breast lesions with higher accuracy.

# Bibliography


[1] Globocan 2020: New global cancer data. Accessed on 26.01.2021. [Online]. Available: https://www.uicc.org/news/globocan-2020-new-global-cancer-data

[2] Canadian cancer statistics advisory committee. Toronto, ON: Canadian Cancer Society, 2019. Accessed on 26.01.2021. [Online]. Available: https://www.cancer.ca/~/media/cancer.ca/CW/cancer%20information/cancer%20101/Canadian%20cancer%20statistics/Canadian-Cancer-Statistics-2019-EN.pdf?la=en

[3] J. Ferlay, M. Ervik, F. Lam, M. Colombet, L. Mery, M. Piñeros, A. Znaor, I. Soerjomataram, and F. Bray. (2020) Global cancer observatory: Cancer today. lyon, france: International agency for research on cancer. Accessed on 26.01.2021. [Online]. Available: https://gco.iarc.fr/today

[4] Breast cancer statistics - canadian cancer society. Accessed on 26.01.2021. [Online]. Available: https://www.cancer.ca/en/cancer-information/cancer-type/breast/statistics/?region=on

[5] Breast cancer facts & figures 2019-2020. American Cancer Society. Accessed on 26.01.2021. [Online]. Available: https://www.cancer.org/content/dam/cancer-org/research/cancer-facts-and-statistics/breast-cancer-facts-and-figures/breast-cancer-facts-and-figures-2019-2020

[6] Department of epidemiology and cancercare manitoba cancer registry. Cancer in Manitoba, 2012 Annual Statistical Report. Accessed on 26.01.2021. [Online]. Available: https://www.cancercare.mb.ca/Research/epidemiology-cancer-registry

[7] World health organization. Accessed on 26.01.2021. [Online]. Available: https://www.who.int/cancer/detection/breastcancer/en/

[8] D. van Der Waal, A. L. Verbeek, G. J. Den Heeten, T. M. Ripping, V. C. Tjan-Heijnen, and M. J. Broeders, "Breast cancer diagnosis and death in the netherlands: a changing burden," *The European Journal of Public Health*, vol. 25, no. 2, pp. 320–324, 2015.

[9] R. M. Mann, J. C. van Zelst, S. Vreemann, and R. D. Mus, "Is ultrafast or abbreviated breast mri ready for prime time?" *Current Breast Cancer Reports*, vol. 11, no. 1, pp. 9–16, 2019.

[10] L. Tabar and P. B. Dean, "A new era in the diagnosis and treatment of breast cancer," *The breast journal*, vol. 16, pp. S2–S4, 2010.

[11] A. M. Hassan and M. El-Shenawee, "Review of electromagnetic techniques for breast cancer detection," *IEEE Reviews in Biomedical Engineering*, vol. 4, pp. 103–118, 2011.

[12] C. T. F. on Preventive Health Care *et al.*, "Recommendations on screening for breast cancer in average-risk women aged 40–74 years," *Cmaj*, vol. 183, no. 17, pp. 1991–2001, 2011.

[13] Canadian cancer society. Accessed on 26.01.2021. [Online]. Available: https://www.cancer.ca/en/cancer-information/diagnosis-and-treatment/tests-and-procedures/mammography/?region=on

[14] B. L. Sprague, R. E. Gangnon, V. Burt, A. Trentham-Dietz, J. M. Hampton, R. D. Wellman, K. Kerlikowske, and D. L. Miglioretti, "Prevalence of mammographically dense breasts in the united states," *JNCI: Journal of the National Cancer Institute*, vol. 106, no. 10, 2014.

[15] M. E. Miller, *Cancer. 1st ed.* Momentum Press, new York, 2018.

[16] P. A. Carney, D. L. Miglioretti, B. C. Yankaskas, K. Kerlikowske, R. Rosenberg, C. M. Rutter, B. M. Geller, L. A. Abraham, S. H. Taplin, M. Dignan *et al.*, "Individual and combined effects of age, breast density, and hormone replacement therapy use on the accuracy of screening mammography," *Annals of internal medicine*, vol. 138, no. 3, pp. 168–175, 2003.

[17] K. McLean and J. Stone, "Role of breast density measurement in screening for breast cancer," *Climacteric*, vol. 21, no. 3, pp. 214–220, 2018.

[18] P. C. Gøtzsche and K. J. Jørgensen, "Screening for breast cancer with mammography," *Cochrane database of systematic reviews*, no. 6, 2013.

[19] E. C. Fear, S. C. Hagness, P. M. Meaney, M. Okoniewski, and M. A. Stuchly, "Enhancing breast tumor detection with near-field imaging," *IEEE Microwave magazine*, vol. 3, no. 1, pp. 48–56, 2002.

[20] E. K. Pauwels, N. Foray, and M. H. Bourguignon, "Breast cancer induced by x-ray mammography screening? a review based on recent understanding of low-dose radiobiology," *Medical Principles and Practice*, vol. 25, no. 2, pp. 101–109, 2016.

[21] K. Hoyt, H. Umphrey, M. Lockhart, M. Robbin, and A. Forero-Torres, "Ultrasound imaging of breast tumor perfusion and neovascular morphology," *Ultrasound in medicine & biology*, vol. 41, no. 9, pp. 2292–2302, 2015.

[22] L. Sim, J. Hendriks, S. Fook-Chong *et al.*, "Breast ultrasound in women with familial risk of breast cancer," *ANNALS-ACADEMY OF MEDICINE SINGAPORE*, vol. 33, no. 5, pp. 600–606, 2004.

[23] C. H. Lee, D. D. Dershaw, D. Kopans, P. Evans, B. Monsees, D. Monticciolo, R. J. Brenner, L. Bassett, W. Berg, S. Feig *et al.*, "Breast cancer screening with imaging: recommendations from the society of breast imaging and the acr on the use of mammography, breast mri, breast ultrasound, and other technologies for the detection of clinically occult breast cancer," *Journal of the American college of radiology*, vol. 7, no. 1, pp. 18–27, 2010.

[24] H.-D. Cheng, J. Shan, W. Ju, Y. Guo, and L. Zhang, "Automated breast cancer detection and classification using ultrasound images: A survey," *Pattern recognition*, vol. 43, no. 1, pp. 299–317, 2010.

[25] C. K. Kuhl, S. Schrading, C. C. Leutner, N. Morakkabati-Spitz, E. Wardelmann, R. Fimmers, W. Kuhn, and H. H. Schild, "Mammography, breast ultrasound, and magnetic resonance imaging for surveillance of women at high familial risk for breast cancer," *Journal of clinical oncology*, vol. 23, no. 33, pp. 8469–8476, 2005.

[26] P. Morrow, Monica, M. Waters, Janet, and P. Morris, Elizabeth, "Mri for breast cancer screening, diagnosis, and treatment," *The Lancet (British edition)*, vol. 378, no. 9805, pp. 1804–1811, 2011.

[27] "An overview of breast mri," *Applied radiology (1976)*, vol. 45, no. 10, pp. 7–, 2016.

[28] R. M. Mann, C. Balleyguier, P. A. Baltzer, U. Bick, C. Colin, E. Cornford, A. Evans, E. Fallenberg, G. Forrai, M. H. Fuchsjäger *et al.*, "Breast mri: Eusobi recommendations for women's information," *European radiology*, vol. 25, no. 12, pp. 3669–3678, 2015.

[29] Z. Haoyu. Microwave imaging for ultra-wideband antenna based cancer detection. The University of Edinburgh, 2014. Accessed on 08.09.2021. [Online]. Available: https://era.ed.ac.uk/bitstream/handle/1842/9958/Zhang2015.

[30] N. R. Council *et al.*, "Mammography and beyond: developing technologies for the early detection of breast cancer," 2001.

[31] N. K. Nikolova, "Microwave imaging for breast cancer," *IEEE microwave magazine*, vol. 12, no. 7, pp. 78–94, 2011.

[32] M. A. Solis Nepote, "Design, development, and evaluation of a clinical system for breast microwave imaging," 2017.

[33] B. M. Moloney, D. O'Loughlin, S. Abd Elwahab, and M. J. Kerin, "Breast cancer detection—a synopsis of conventional modalities and the potential role of microwave imaging," *Diagnostics*, vol. 10, no. 2, p. 103, 2020.

[34] S. C. Hagness, A. Taflove, and J. E. Bridges, "Two-dimensional fdtd analysis of a pulsed microwave confocal system for breast cancer detection: Fixed-focus and antenna-array sensors," *IEEE transactions on biomedical engineering*, vol. 45, no. 12, pp. 1470–1479, 1998.

[35] P. T. Huynh, A. M. Jarolimek, and S. Daye, "The false-negative mammogram." *Radiographics*, vol. 18, no. 5, pp. 1137–1154, 1998.

[36] A. Vander Vorst, A. Rosen, and Y. Kotsuka, *RF/microwave interaction with biological tissues*. Wiley Online Library, 2006, vol. 181.

[37] M. M. Rana, "Development and evaluation of a sensor and antenna array for a portable microwave-based breast cancer detection system," 2021.

[38] T. Reimer, “Improving image reconstruction and machine learning methods in breast microwave sensing,” 2020.

[39] A. Martellosio, M. Pasian, M. Bozzi, L. Perregrini, A. Mazzanti, F. Svelto, P. E. Summers, G. Renne, L. Preda, and M. Bellomi, “Dielectric properties characterization from 0.5 to 50 ghz of breast cancer tissues,” *IEEE Transactions on Microwave Theory and Techniques*, vol. 65, no. 3, pp. 998–1011, 2016.

[40] L. Sha, E. R. Ward, and B. Stroy, “A review of dielectric properties of normal and malignant breast tissue,” in *Proceedings IEEE SoutheastCon 2002 (Cat. No. 02CH37283)*. IEEE, 2002, pp. 457–462.

[41] T. Sugitani, S.-i. Kubota, S.-i. Kuroki, K. Sogo, K. Arihiro, M. Okada, T. Kadoya, M. Hide, M. Oda, and T. Kikkawa, “Complex permittivities of breast tumor tissues obtained from cancer surgeries,” *Applied Physics Letters*, vol. 104, no. 25, p. 253702, 2014.

[42] M. Solis-Nepote, T. Reimer, and S. Pistorius, “An air-operated bistatic system for breast microwave radar imaging: pre-clinical validation,” in *2019 41st Annual International Conference of the IEEE Engineering in Medicine and Biology Society (EMBC)*. IEEE, 2019, pp. 1859–1862.

[43] P. M. Meaney, M. W. Fanning, D. Li, S. P. Poplack, and K. D. Paulsen, “A clinical prototype for active microwave imaging of the breast,” *IEEE Transactions on Microwave Theory and Techniques*, vol. 48, no. 11, pp. 1841–1853, 2000.

[44] E. C. Fear, J. Bourqui, C. Curtis, D. Mew, B. Docktor, and C. Romano, “Microwave breast imaging with a monostatic radar-based system: A study of application to patients,” *IEEE transactions on microwave theory and techniques*, vol. 61, no. 5, pp. 2119–2128, 2013.

[45] E. Porter, E. Kirshin, A. Santorelli, M. Coates, and M. Popović, “Time-domain multistatic radar system for microwave breast screening,” *IEEE Antennas and Wireless Propagation Letters*, vol. 12, pp. 229–232, 2013.

[46] A. W. Preece, I. Craddock, M. Shere, L. Jones, and H. L. Winton, "Maria m4: clinical evaluation of a prototype ultrawideband radar scanner for breast cancer detection," *Journal of Medical Imaging*, vol. 3, no. 3, p. 033502, 2016.

[47] E. C. Fear, X. Li, S. C. Hagness, and M. A. Stuchly, "Confocal microwave imaging for breast cancer detection: Localization of tumors in three dimensions," *IEEE Transactions on biomedical engineering*, vol. 49, no. 8, pp. 812–822, 2002.

[48] H. B. Lim, N. T. T. Nhung, E.-P. Li, and N. D. Thang, "Confocal microwave imaging for breast cancer detection: Delay-multiply-and-sum image reconstruction algorithm," *IEEE Transactions on Biomedical Engineering*, vol. 55, no. 6, pp. 1697–1704, 2008.

[49] S. V. Sree, E. Y.-K. Ng, R. U. Acharya, and O. Faust, "Breast imaging: a survey," *World journal of clinical oncology*, vol. 2, no. 4, p. 171, 2011.

[50] T. M. Grzegorczyk, P. M. Meaney, P. A. Kaufman, K. D. Paulsen *et al.*, "Fast 3-d tomographic microwave imaging for breast cancer detection," *IEEE transactions on medical imaging*, vol. 31, no. 8, pp. 1584–1592, 2012.

[51] R. Nilavalan, I. Craddock, A. Preece, J. Leendertz, and R. Benjamin, "Wideband microstrip patch antenna design for breast cancer tumour detection," *IET Microwaves, Antennas & Propagation*, vol. 1, no. 2, pp. 277–281, 2007.

[52] D. O'Loughlin, B. L. Oliveira, M. Glavin, E. Jones, and M. O'Halloran, "Advantages and disadvantages of parameter search algorithms for permittivity estimation for microwave breast imaging," in *2019 13th European Conference on Antennas and Propagation (EuCAP)*. IEEE, 2019, pp. 1–5.

[53] T. Reimer, J. Sacristan, and S. Pistorius, "Improving the diagnostic capability of microwave radar imaging systems using machine learning," in *2019 13th European Conference on Antennas and Propagation (EuCAP)*. IEEE, 2019, pp. 1–5.

[54] J. Bourqui, J. M. Sill, and E. C. Fear, "A prototype system for measuring microwave frequency reflections from the breast," *International journal of biomedical imaging*, vol. 2012, 2012.

[55] N. Epstein, P. Meaney, and K. Paulsen, "3d parallel-detection microwave tomography for clinical breast imaging," *Review of Scientific Instruments*, vol. 85, no. 12, p. 124704, 2014.

[56] E. Porter, E. Kirshin, A. Santorelli, M. Coates, and M. Popović, "Time-domain multistatic radar system for microwave breast screening," *IEEE Antennas and Wireless Propagation Letters*, vol. 12, pp. 229–232, 2013.

[57] Q. Fang, P. M. Meaney, and K. D. Paulsen, "Viable three-dimensional medical microwave tomography: Theory and numerical experiments," *IEEE transactions on antennas and propagation*, vol. 58, no. 2, pp. 449–458, 2009.

[58] J. Bourqui, M. Okoniewski, and E. C. Fear, "Balanced antipodal vivaldi antenna with dielectric director for near-field microwave imaging," *IEEE Transactions on Antennas and Propagation*, vol. 58, no. 7, pp. 2318–2326, 2010.

[59] M. Klemm, D. Gibbins, J. Leendertz, T. Horseman, A. Preece, R. Benjamin, and I. Craddock, "Development and testing of a 60-element uwb conformal array for breast cancer imaging," in *Proceedings of the 5th European Conference on Antennas and Propagation (EUCAP)*. IEEE, 2011, pp. 3077–3079.

[60] D. Flores-Tapia, D. Rodriguez, M. Solis, N. Kopotun, S. Latif, O. Maizlish, L. Fu, Y. Gui, C.-M. Hu, and S. Pistorius, "Experimental feasibility of multistatic holography for breast microwave radar image reconstruction," *Medical physics (Lancaster)*, vol. 43, no. 8, pp. 4674–4686, 2016.

[61] T. Reimer, M. Solis-Nepote, and S. Pistorius, "The application of an iterative structure to the delay-and-sum and the delay-multiply-and-sum beamformers in breast microwave imaging," *Diagnostics*, vol. 10, no. 6, p. 411, 2020.

[62] S. C. Hagness, A. Taflove, and J. E. Bridges, "Three-dimensional fdtd analysis of a pulsed microwave confocal system for breast cancer detection: Design of an antenna-array element," *IEEE Transactions on Antennas and Propagation*, vol. 47, no. 5, pp. 783–791, 1999.

[63] T. Rubæk, O. S. Kim, and P. Meincke, "Computational validation of a 3-d microwave imaging system for breast-cancer screening," *IEEE Transactions on Antennas and Propagation*, vol. 57, no. 7, pp. 2105–2115, 2009.

[64] D. Gibbins, M. Klemm, I. J. Craddock, J. A. Leendertz, A. Preece, and R. Benjamin, "A comparison of a wide-slot and a stacked patch antenna for the purpose of breast cancer detection," *IEEE transactions on antennas and propagation*, vol. 58, no. 3, pp. 665–674, 2009.

[65] B. J. Mohammed, A. M. Abbosh, and P. Sharpe, "Planar array of corrugated tapered slot antennas for ultrawideband biomedical microwave imaging system," *International Journal of RF and Microwave Computer-Aided Engineering*, vol. 23, no. 1, pp. 59–66, 2013.

[66] M. T. Islam, M. Z. Mahmud, N. Misran, J. Takada, and M. Cho, "Microwave breast phantom measurement system with compact side slotted directional antenna," *IEEE Access*, vol. 5, pp. 5321–5330, 2017.

[67] E. Avşar Aydin, "A preliminary study for early breast cancer detection with microwaves," *Tehnički glasnik*, vol. 12, no. 2, pp. 109–112, 2018.

[68] S. M. Chouiti, L. Merad, S. M. Meriah, X. Raimundo, and A. Taleb-Ahmed, "An efficient image reconstruction method for breast cancer detection using an ultra-wideband microwave imaging system," *Electromagnetics*, vol. 36, no. 4, pp. 225–235, 2016.

[69] A. Aydin and E. Avşar Aydin, "Evaluation of limestone layer's effect for uwb microwave imaging of breast models using neural network," *Tehnički glasnik*, vol. 11, no. 1-2, pp. 50–54, 2017.

[70] A. F. Yahya, Y. M. Abbosh, and A. Abbosh, "Microwave imaging method employing wavelet transform and neural networks for breast cancer detection," in *Asia-Pacific Microwave Conference 2011*. IEEE, 2011, pp. 1418–1421.

[71] E. A. Aydin and M. K. Keleş, "Uwb rectangular microstrip patch antenna design in matching liquid and evaluating the classification accuracy in data mining using random forest algorithm for breast cancer detection with microwave," *Journal of Electrical Engineering & Technology*, vol. 14, no. 5, pp. 2127–2136, 2019.

[72] F. Rauf, K. S. Anderson, and J. LaBaer, "Autoantibodies in early detection of breast cancer," *Cancer epidemiology, biomarkers and prevention*, vol. 29, no. 12, pp. 2475–2485, 2020.

[73] J. Sacristan, "Preliminary study of a mobile microwave breast cancer detection device using machine learning," 2017.

[74] J. Sacristán and S. Pistorius, "A comparison of classifiers for detecting tumours using microwave scattering in numerical breast models," *CMBES Proceedings*, vol. 40, 2017.

[75] J. Sacristán, B. L. Oliveira, and S. Pistorius, "Classification of electromagnetic signals obtained from microwave scattering over healthy and tumorous breast models," in *2016 IEEE Canadian Conference on Electrical and Computer Engineering (CCECE)*. IEEE, 2016, pp. 1–5.

[76] Cst studio suite 3d em simulation and analysis software. Accessed on 02.10.2021. [Online]. Available: https://www.3ds.com/products-services/simulia/products/cst-studio-suite/

[77] Antenna magus - antenna design software. Accessed on 02.10.2021. [Online]. Available: https://www.3ds.com/products-services/simulia/products/antenna-magus/

[78] 2-20ghz broadband horn antenna. Accessed on 02.10.2021. [Online]. Available: http://www.ainfoinc.com.cn/en/p_ant_h_brd.asp

[79] S. I. Latif, D. Flores Tapia, D. Rodriguez Herrera, M. Solis Nepote, S. Pistorius, and L. Shafai, "A directional antenna in a matching liquid for microwave radar imaging," *International Journal of Antennas and Propagation*, vol. 2015, 2015.

[80] D. T. Al-Zuhairi, J. M. Gahl, and N. E. Islam, "Compact dual-polarized quad-ridged uwb horn antenna design for breast imaging," *Progress In Electromagnetics Research*, vol. 72, pp. 133–140, 2017.

[81] M. Ghorbani and A. Khaleghi, "Double ridged horn antenna designs for wideband applications," in *2011 19th Iranian Conference on Electrical Engineering*. IEEE, 2011, pp. 1–4.

[82] M. S. Nepote, D. R. Herrera, D. F. Tapia, S. Latif, and S. Pistorius, "A comparison study between horn and vivaldi antennas for 1.5–6 ghz breast microwave radar imaging," in *The 8th European Conference on Antennas and Propagation (EuCAP 2014)*. IEEE, 2014, pp. 59–62.

[83] Tablecurve 3d. Accessed on 14.05.2021. [Online]. Available: https://www.environmentalexpert.com/software/tablecurve-3d-version-40-automoted-curve-fitting-analysis-software-598